Article

JOURNAL OF COMPOSITE MATERIALS

Journal of Composite Materials
0(0) 1–23

DOI: 10.1177/0021998310392412
jcm.sagepub.com

SAGE

Modeling the effects of stress concentrations on the initiation of matrix cracking in woven CMCs

M.P. Rao[1,2], M. Pantiuk[1] and P.G. Charalambides[1]

Abstract

In this study, we employ detailed three-dimensional (3D) finite element models of plain and satin weave ceramic matrix composites (CMCs) as needed to establish the stress concentration around existing voids and their effect on the elastic response of these complex material systems. Fundamental 3D elasticity boundary value problems addressing the response of these materials under a combination of remote biaxial tension, in-plane shear, and thermal loading are utilized to characterize the matrix micro-stresses in the vicinity of large-scale macroscopic voids. The combined stress fields are then used to assess the conditions for the initiation of matrix cracking in such regions of high-stress concentration. Comparison of model results with available experimental data is discussed. Extensive parametric studies have yielded broad matrix cracking loci, which may be critical for the reliable use of woven CMCs in engineering applications.

Keywords

ceramic matrix composites, strength, finite element analysis, stress concentrations, micro-mechanics

Introduction

Woven fabric composites can be engineered to provide high strength and toughness in comparison with conventional monolithic materials for a wide variety of land-, sea- and space-based applications. However, these materials are characterized by a complicated three-dimensional (3D) geometry and intricate microstructures.[1–13] As such, intricate solution techniques are needed to perform the stress analysis of such materials and quantify the mechanisms which drive ultimate failure in these systems.

When woven ceramic matrix composites (CMCs) are loaded in-plane, micro-failure events such as matrix micro-cracking, fiber debonding, fiber crack surface bridging, frictional fiber pull-out, and fiber tow delamination have been shown to occur.[14,15] Such systems often exhibit a nonlinear stress–strain curve characterized by a graceful ultimate failure.[15] Under the influence of high-temperature gradients, the strength of woven CMCs has been shown to decrease mainly due to the presence of thermal stresses induced during processing and operating temperature changes. Such residual stresses are often amplified by the mismatch in the coefficients of thermal expansion (CTEs) between the fibers and matrix material.[16] In most engineering applications, the Proportional Limit (PL) also known as 'the first knee' on the stress–strain curve, is used as the guiding design criterion. This 'first knee' has been shown to coincide with the 'first matrix cracking' stress identified as the PL of the woven composite material.[17] In Haan[17] and Kuhn et al.[18] a progressive stress-induced micro-cracking damage model is employed to study the stress-induced damage evolution in Plain Weave (PW) CMC systems. Those studies clearly showed that upon initiation of micro-cracking damage at sites of stress concentration, the apparent stress–strain curve exhibits its first deviation from

[1]Department of Mechanical Engineering, The University of Maryland, Baltimore County, 1000 Hilltop Circle, Baltimore, MD 21250, USA.
[2]Center for Composite Materials, University of Delaware, Newark, DE 19716, USA.

Corresponding author:
M.P. Rao, Department of Mechanical Engineering, The University of Maryland, Baltimore County, 1000 Hilltop Circle, Baltimore, MD 21250, USA; Center for Composite Materials, University of Delaware, Newark, DE 19716, USA
Email: mprao@udel.edu

linearity. The study also showed that the 'knee' of the apparent stress–strain curve becomes more pronounced in systems capable of higher saturation damage densities. In light of the above, the linear fields are employed in this study to identify the end of the linear regime, which we define as the PL.

In addition, experimental stress–strain curves of various woven CMCs, reported in Morscher[12,13] and Smith et al.[19] clearly indicate the presence of a 'knee' delineating the linear and the non-linear regions of the composite's macro-mechanical response. Employing modal Acoustic Emission (AE) techniques, it was shown in Morscher[12] that, low-energy AE events correspond with the formation of matrix micro-cracks within the linear regions of the response. High-energy AE events on the other hand,[12] indicate coalescence or bridging of large matrix cracks that propagate in the through-thickness direction. In particular, Morscher[12] linked the onset of nonlinearity with the above high-energy AE events. The stress corresponding to the 'knee' in the stress–strain curves could be regarded as the PL strength of woven CMCs, associated with high-energy AE events.

Thus, from the standpoint of engineering design, the PL stress of woven CMCs is a parameter of critical importance. Therefore, the objective of this study is to develop broad matrix cracking failure loci for plain and satin weave C/SiC systems subjected to a combination of in-plane mechanical and thermal loads often induced during cooling due to thermal expansion mismatches between the fiber and matrix phases.

Geometric modeling and material properties

The representative 3D finite element meshes of the repeating unit-cells of woven CMCs described in this study are illustrated in Figures 1 and 2. In particular, Figure 1(a) and (b) represents the PW and Four Harness (4HS) satin weave architectures, whereas

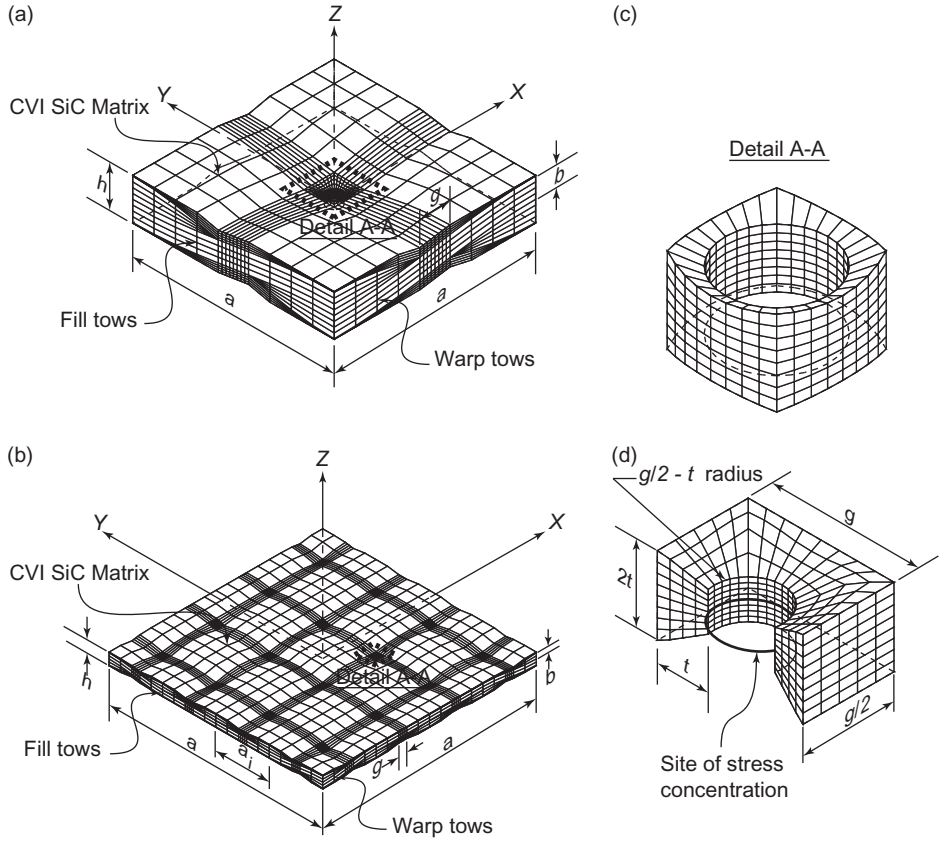

Figure 1. Representative finite element meshes of the PW and Four Harness satin weave CMCs employed to address fundamental thermo-elastic boundary value problems. (a) and (b) Finite element meshes displaying the layered structure of the PW and Four Harness satin weave CMCs, respectively, along with the definitions of the corresponding spatial geometric parameters used to construct the meshes. (c) A blow-up of the element set containing the finite elements closest to the individual chosen matrix voids in the unit-cell. (d) Section of the central matrix void showing the region of stress concentration. The thick solid circle represents the location at which the stresses are extracted.

Figure 2(a) and (b) depicts the Five Harness (5HS) and Eight Harness (8HS) satin weave morphologies. Furthermore in Figures 1 and 2, parts (c) and (d) bring to light, the geometric details of local macroscopic matrix voids chosen for stress averaging as would be discussed in a later section. The normalized geometry parameters utilized to construct the individual finite element meshes in Figures 1 and 2 are listed in Table 1(Panel A). The 3D finite element meshes employed herein were developed based on the geometry normalization scheme and tow and matrix layer mathematical surface functions presented in Rao et al.[20]

The study presented by Morscher[13] includes multiple micro-graphs of woven CVI CMCs, wherein the spatial distribution of macroscopic voids is either evident or could be easily inferred. As reported elsewhere,[21] these repeating unit-cell models have been employed to predict undamaged effective elastic properties of woven CVI CMCs, which, as reported in Rao[21] were shown to be in excellent agreement with experimental data.

The fiber tows in woven CMCs constitute hierarchical material entities with directional properties. Due to this complexity, we need to employ the homogenized thermal properties of fiber tows in the finite element model. The fibers in general, could be modeled as transversely isotropic with E_L^f, ν_{LT}^f, and G_{LT}^f representing the fiber longitudinal elastic modulus, and in-plane Poisson's ratio, and shear modulus. Similarly, E_T^f, ν_{TL}^f, and G_{TL}^f represent the fiber transverse elastic modulus, and reciprocal in-plane Poisson's ratio, and shear modulus, respectively. The fiber coating around the fibers is modeled as an isotropic material entity with elastic modulus E_{fc} and Poisson's ratio ν_{fc}. Owing to the CVI process of ceramic matrix deposition, the matrix within bundles (bundle matrix) and the matrix material surrounding bundles (inter-bundle matrix) are

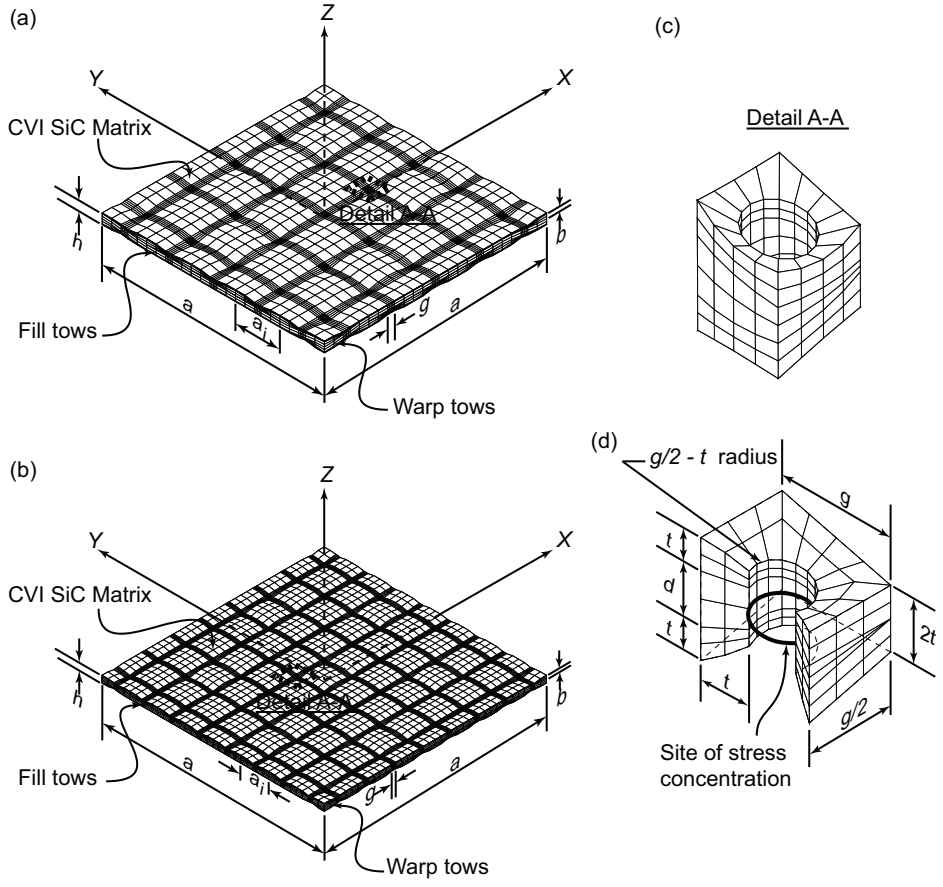

Figure 2. Representative finite element meshes of the Five Harness and Eight Harness satin weave CMCs employed to address fundamental thermo-elastic boundary value problems. (a) and (b) Finite element meshes displaying the layered structure of the Five Harness and Eight Harness satin weave CMCs, respectively, along with the definitions of the corresponding spatial geometric parameters used to construct the meshes. (c) A blow-up of the element set containing the finite elements closest to the individual chosen matrix voids in the unit-cell. (d) Section of the central matrix void showing the region of stress concentration. The thick solid circle represents the location at which the stresses are extracted.

Table 1. The input geometry parameters, physical and micro-structural material properties of the C/SiC woven CMCs modeled in this study

Panel A: Normalized micro-structural input geometry parameters

PW geometry	Satin weave geometry
$\hat{a} = 1.0$	$\hat{a} = 1.0$
$\hat{b} = 0.1$	$\hat{a}_i = 0.25, 0.2, 0.125$
$\hat{g} = 0.15$	$\hat{b} = 0.1\,\hat{a}_i$
$\hat{t} = 0.04$	$\hat{g} = 0.15\,\hat{a}_i$
$\hat{h} = 2.0\,\hat{b}$	$\hat{t} = 0.04\,\hat{a}_i$
	$\hat{h} = 2.0\,\hat{b}$

Panel B: Normalized micro-structural input material parameters[17]

Fiber	Fiber coating	Matrix	Bundle coating	Volume fractions
				$v_{f/b} = 0.75$
				$v_{fc/b} = 0.05$
$\hat{E}_f = 0.8$	$\hat{E}_{fc} = 0.125$	$\hat{E}_m = 1.0$	$\hat{E}_{bc} = 0.25$	$v_{bm/b} = 0.14$
$v_f = 0.43$	$v_{fc} = 0.25$	$v_m = 0.3$	$v_{bc} = 0.25$	$v_{bc/b} = 0.05$
$\hat{a}_f = 0.3$	$\hat{a}_{fc} = 1.0$	$\hat{a}_m = 1.0$	$\hat{a}_{bc} = 1.0$	$v_{bp/b} = 0.01$
				$v_{m/m} = 0.9$
				$v_{mp/m} = 0.1$

Panel C: Physical properties of the PW C/SiC systems[17]

Entity	Description
Fiber	Toray T-300 1K tow carbon fiber
Matrix	SiC
Tensile strength	300–400 MPa
Fiber content	40% by volume
Process	Chemical vapor infiltration (CVI)
Modulus	Not available
Composite PL	80 MPa (tensile)

the same. Therefore, the bundle and inter-bundle matrix materials are modeled as isotropic with elastic modulus E_m and Poisson's ratio v_m, respectively. Finally, the bundle coating is also modeled as an isotropic medium with elastic modulus E_{bc} and Poisson's ratio v_{bc}.

Effective thermal properties of the fiber tows were computed with the aid of the study presented by Chamis.[22] In Chamis,[22] the author derived closed-form expressions for the effective longitudinal (α_L) and transverse (α_T) CTEs of an unidirectionally reinforced composite lamina with transversely isotropic fibers embedded in an isotropic matrix. Transversely isotropic fibers could be modeled with α_L^f and α_T^f representing the fiber longitudinal and transverse CTE, respectively. Similarly, the isotropic matrix material could be modeled with α_m representing coefficient of thermal expansion. Then, based on simple force balance, the effective longitudinal and transverse CTEs of the lamina are given by:[22]

$$\begin{aligned} \alpha_L &= \frac{c_f \alpha_L^f E_L^f + c_m \alpha_m E_m}{E_L^\ell} \\ \alpha_T &= \alpha_T^f \sqrt{c_f} + \left(1 - \sqrt{c_f}\right)\left(1 + c_f v_m \frac{E_L^f}{E_L^\ell}\right)\alpha_m \end{aligned} \tag{1}$$

where

$$E_L^\ell = c_f E_L^f + c_m E_m \tag{2}$$

In Equations (1) and (2), E_L^ℓ represents the rule-of-mixtures effective longitudinal elastic modulus of the lamina and c_f and c_m are the volume fractions

of the fiber and matrix phases, respectively. The elastic moduli and Poisson's ratios entering into Equations (1) and (2) were described above. We employ Equation (1) in the four-step homogenization procedure developed by Kuhn and Charalambides[23] to determine the effective longitudinal and transverse CTEs of the fiber tows.

During each step of the homogenization procedure, appropriate magnitudes for c_f and c_m are substituted in Equations (1) and (2) consistent with.[23] Additionally, the elastic and thermal properties appearing in Equations (1) and (2) are set equal to the corresponding magnitudes of individual material micro-constituents considered in each step of the homogenization procedure. These normalized input microstructural material properties are reported in Table 1(Panel B). The 'hat' (ˆ) notation in Table 1(Panel B) corresponding to a modulus signifies that the property has been normalized with respect to the matrix elastic modulus E_m, whereas the 'hat' (ˆ) notation for a CTE value implies that it has been normalized with respect to the matrix CTE α_m.

Of particular interest is the homogenization of the porous bundle and inter-bundle matrix phases. Since porosity assumes the same CTE as that of the surrounding medium, the effective CTE of the effective isotropic bundle matrix is computed with the aid of a simple rule-of-mixtures approach. In particular, we have

$$\alpha_{\overline{bm}} = \frac{c_f \alpha_f E_f + c_m \alpha_m E_m}{E_L^{\ell}} \tag{3}$$

where E_L^{ℓ} is given by Equation (2) and E_f and E_m symbolically represent the elastic moduli of the fiber and matrix phases, respectively. Further, in Equation (3), α_f and α_m represent the CTEs of the fiber and matrix phases, respectively. In the above formulation, we consider the micro-voids in the bundle matrix to represent the 'fibers'. As such, substituting appropriate magnitudes for c_f and c_m consistent with Kunn and Charalambides[23] and recognizing that porosity has a zero elastic modulus, the expression for the effective CTE of the bundle matrix reduces to $\alpha_{\overline{bm}} = \alpha_m$. Using a similar argument, it could be shown that the effective CTE of the inter-bundle matrix phase is given by $\alpha_{\overline{m}} = \alpha_m$.

The volume fractions of the micro-constituents in Table 1(Panel B) are listed with respect to the volume occupied by the bundles and inter-bundle matrix within the repeating unit-cells of the woven CMCs. For example, the notation $v_{f/b}$ in Table 1(Panel B) implies the volume fraction of the fibers within the fiber bundles in the repeating unit-cells, whereas the notation $v_{m/m}$ indicates the volume fraction of the matrix within the inter-bundle matrix. Note that the term inter-bundle matrix here means the material phase that includes matrix as well as porosity occupying the region between bundles not including the large scale matrix voids.

Table 2. The output meso- and macroscopic material properties of the PW and 5HS satin weave C/SiC CMCs modeled in this study

Effective tow	Effective matrix	Overall volume fractions	Undamaged unit-cell
Panel A: PW meso- and macroscopic outputs			
$\hat{E}_{11} = 0.752$			
$\hat{E}^{\ell}_{22} = 0.636$			
$\hat{G}_{12} = 0.239$	$\hat{E}_{\bar{m}} = 0.810$	$v_{fill} = 0.271$	$\hat{E}_{xx} = 0.606$
$\hat{G}^{\ell}_{23} = 0.230$	$\hat{G}_{\bar{m}} = 0.288$	$v_{warp} = 0.271$	$\hat{E}_{yy} = 0.606$
$v_{12} = 0.397$	$v_{\bar{m}} = 0.314$	$v_{matrix} = 0.316$	$v_{xy} = 0.324$
$v^{\ell}_{23} = 0.379$	$\hat{a}_{\bar{m}} = 1.0$	$v_{void} = 0.142$	$v_{yx} = 0.324$
$\hat{a}_{11} = 0.454$			$\hat{G}_{xy} = 0.217$
$\hat{a}_{22} = 0.229$			
Panel B: Five Harness satin weave meso and macroscopic outputs			
$\hat{E}_{11} = 0.752$			
$\hat{E}^{\ell}_{22} = 0.636$			
$\hat{G}_{12} = 0.239$	$\hat{E}_{\bar{m}} = 0.810$	$v_{fill} = 0.271$	$\hat{E}_{xx} = 0.644$
$\hat{G}^{\ell}_{23} = 0.230$	$\hat{G}_{\bar{m}} = 0.288$	$v_{warp} = 0.271$	$\hat{E}_{yy} = 0.644$
$v_{12} = 0.397$	$v_{\bar{m}} = 0.314$	$v_{matrix} = 0.391$	$v_{xy} = 0.310$
$v^{\ell}_{23} = 0.379$	$\hat{a}_{\bar{m}} = 1.0$	$v_{void} = 0.067$	$v_{yx} = 0.310$
$\hat{a}_{11} = 0.454$			$\hat{G}_{xy} = 0.233$
$\hat{a}_{22} = 0.229$			

The volume fractions and constituent properties listed in Table 1(Panel B) are used in the above-mentioned four-step homogenization procedure to compute the effective thermo-elastic properties of the orthotropic fiber bundles in the principal material directions (PMDs). The homogenized material properties of the inter-bundle matrix phase upon accounting for the dispersed porosity are employed to compute the material properties of the effective matrix. As such, the 'Effective Tow' and 'Effective Matrix' columns in Table 2 list the results of the homogenization procedure. The volume fractions of the tows, matrix and large-scale matrix voids computed with the aid of geometry surface functions[20] are listed under 'Overall Volume Fractions' in Table 2. The effective elastic properties of the woven CMCs computed with the aid of 3D finite element macro-level unit-strain boundary value problems[21,23,24] are listed under the heading 'Undamaged Unit-Cell' in Table 2.

Model formulation – combined mechanical and thermal effects

Total stress function

The application of in-plane mechanical loads is conveniently represented in this study via the macroscopic stresses σ_{xx}^{∞}, σ_{yy}^{∞}, and τ_{xy}^{∞} or via the spherical loading parameters, ω, ϕ, and S, as shown in Figure 3. The remotely applied in-plane mechanical loads can be related to the spherical loading parameters as follows:

$$\begin{aligned}\sigma_{xx}^{\infty} &= S\cos\phi\cos\omega \\ \sigma_{yy}^{\infty} &= S\cos\phi\sin\omega \\ \tau_{xy}^{\infty} &= S\sin\phi\end{aligned} \tag{4}$$

where S represents the combined mechanical loading stress magnitude and ϕ and ω represent the loading phase angles. For example, when S is nonzero and $\phi=\omega=0$, the loading case collapses to the X-direction uniaxial tension case. The $S\neq 0$ and $\phi=90^{\circ}$ case represents in-plane pure shear loading.

It has been shown in previous studies[18,25] that the total stress induced in the woven CMC scales linearly with the remotely applied loads. Let σ_{ij}^{x} be the ij-component of the stress tensor induced due to uniaxial tension along the global X-direction and σ_{ij}^{y} be the ij-component of the stress tensor induced due to uniaxial tension along the global Y-direction. Similarly, we set τ_{ij}^{xy} to be the induced ij-component of the stress tensor due to pure remote in-plane shear loading and σ_{ij}^{th} to be the induced ij-component of the stress tensor due to free thermal expansion. Based on the principle of linear superposition, the total ij-component of the stress tensor is given by:

$$\sigma_{ij}^{total} = \sigma_{ij}^{x} + \sigma_{ij}^{y} + \tau_{ij}^{xy} + \sigma_{ij}^{th} \tag{5}$$

Each of the individual stress components on the right-hand side of Equation (5) can be related to the remotely applied mechanical or thermal load as follows:

$$\begin{aligned}\sigma_{ij}^{x} &= \hat{\sigma}_{ij}^{x}\sigma_{c}^{x} \\ \sigma_{ij}^{y} &= \hat{\sigma}_{ij}^{y}\sigma_{c}^{y} \\ \tau_{ij}^{xy} &= \hat{\sigma}_{ij}^{xy}\sigma_{c}^{xy} \\ \sigma_{ij}^{th} &= \hat{\sigma}_{ij}^{th}\sigma_{c}^{th}\end{aligned} \tag{6}$$

where σ_{c}^{x}, σ_{c}^{y}, σ_{c}^{xy}, and σ_{c}^{th} are the characteristic stresses associated with their respective nondimensional finite element boundary value problems considered in this study. More specifically, the subscript 'c' is used to denote that the related stress is a characteristic stress whereas the superscript denotes the associated direction of remote loading. Thus, σ_{c}^{x} denotes the characteristic stress associated with remote tension in the X-direction.

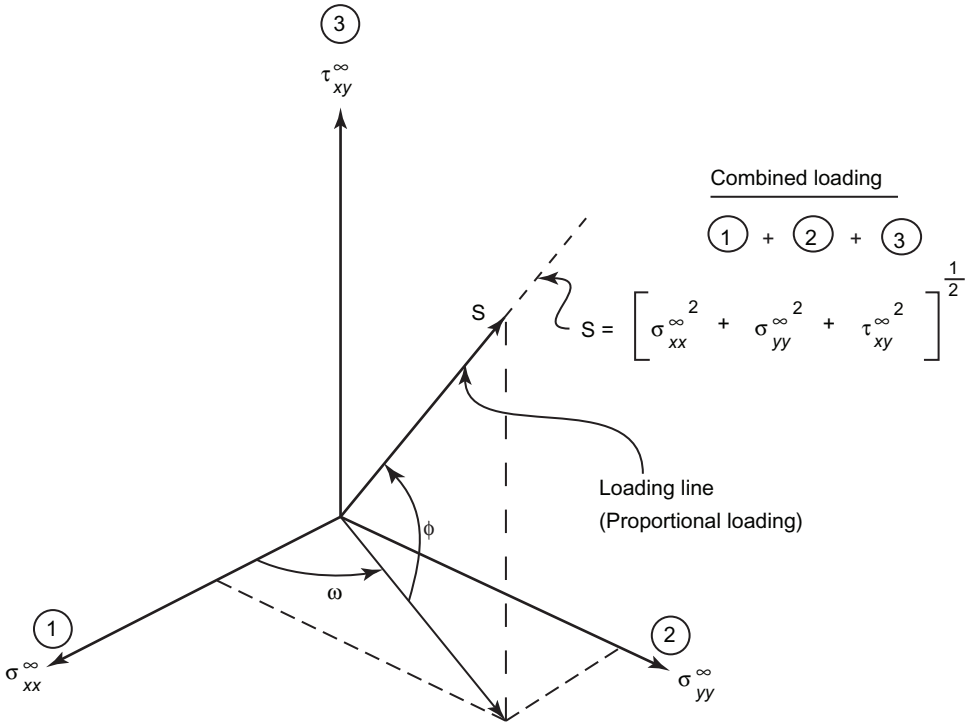

Figure 3. A schematic of the mechanical loading space showing the spherical loading parameters ω, ϕ, and S.

As discussed elsewhere,[21] and since the boundary value problems used in deriving the stress profiles reported herein were formulated as displacement control problems, the above characteristic stresses are then expressed in terms of the applied remote stress σ_{xx}^{∞}, σ_{yy}^{∞}, τ_{xy}^{∞}, and thermal stress $\sigma_{th}^{\infty} = E_c\alpha_c\Delta T_c$ as follows:

$$\begin{aligned}\sigma_c^x &= \sigma_{xx}^{\infty}/\hat{E}_{xx}\\ \sigma_c^y &= \sigma_{yy}^{\infty}/\hat{E}_{yy}\\ \sigma_c^{xy} &= \tau_{xy}^{\infty}/\hat{G}_{xy}\\ \sigma_c^{th} &= \sigma_{th}^{\infty} = E_c\alpha_c\Delta T_c\end{aligned} \tag{7}$$

with $\hat{E}_{xx}$, $\hat{E}_{yy}$ being the effective elastic moduli in the X- and Y-directions, respectively, and $\hat{G}_{xy}$ being the effective modulus of the systems under consideration. Also in the above equation, E_c, α_c, and ΔT_c represent the characteristic or reference modulus, CTE, and temperature change.

In this study, we choose the inter-bundle matrix material with elastic modulus E_m and CTE α_m as the characteristic material phase in the woven system. Further, the 'hat' ($\hat{}$) notation over a stress component in Equation (6) implies that the particular component of stress is the normalized nondimensional stress computed from the finite element solution. Substituting Equations (6) and (7) into Equation (5), we have:

$$\sigma_{ij}^{total} = \hat{\sigma}_{ij}^x\frac{\sigma_{xx}^{\infty}}{\hat{E}_{xx}} + \hat{\sigma}_{ij}^y\frac{\sigma_{yy}^{\infty}}{\hat{E}_{yy}} + \hat{\sigma}_{ij}^{xy}\frac{\tau_{xy}^{\infty}}{\hat{G}_{xy}} + \hat{\sigma}_{ij}^{th}E_c\alpha_c\Delta T_c \tag{8}$$

By combining Equations (4) and (8), the combined total stress due to the simultaneous application of axial loading in the X-, Y-, and XY-directions along with thermal loading takes the form:

$$\begin{aligned}\sigma_{ij}^{total} = {} & S\left(\frac{E_m}{E_{xx}}\right)\cos\phi\cos\omega\,\hat{\sigma}_{ij}^x + S\left(\frac{E_m}{E_{yy}}\right)\cos\phi\sin\omega\,\hat{\sigma}_{ij}^y\\ & + S\left(\frac{E_m}{G_{xy}}\right)\sin\phi\,\hat{\sigma}_{ij}^{xy} + E_c\alpha_c\Delta T_c\hat{\sigma}_{ij}^{th}\end{aligned} \tag{9}$$

where E_m is the elastic modulus of the matrix material and E_{xx}, E_{yy}, and G_{xy} the elastic and shear moduli of the particular woven system. Normalizing Equation (9) with respect to the remotely applied mechanical stress S, we get:

$$\begin{aligned}\sigma_{ij}^{total} = S\Bigg[& \left(\frac{1}{\hat{E}_{xx}}\right)\cos\phi\cos\omega\,\hat{\sigma}_{ij}^x + \left(\frac{1}{\hat{E}_{yy}}\right)\cos\phi\sin\omega\,\hat{\sigma}_{ij}^y\\ & + \left(\frac{1}{\hat{G}_{xy}}\right)\sin\phi\hat{\sigma}_{ij}^{xy} + \beta\hat{\sigma}_{ij}^{th}\Bigg]\end{aligned} \tag{10}$$

where

$$\begin{aligned}\hat{E}_{xx} &= \frac{E_{xx}}{E_m}\\ \hat{E}_{yy} &= \frac{E_{yy}}{E_m}\\ \hat{G}_{xy} &= \frac{G_{xy}}{E_m}\end{aligned} \tag{11}$$

and

$$\beta = \frac{E_c\alpha_c\Delta T_c}{S} \tag{12}$$

is defined as the loading proportionality constant, which measures the ratio of the applied thermal and mechanical loads. Consequently, a very advantageous functional relationship for the total induced stress has been achieved which can be written as:

$$\sigma_{ij}^{total} = S\hat{\Sigma}_{ij}^{total}\left(\phi,\omega,\beta,\hat{\sigma}_{ij}^x,\hat{\sigma}_{ij}^y,\hat{\sigma}_{ij}^{xy},\hat{\sigma}_{ij}^{th}\right) \tag{13}$$

In Equation (13), $\hat{\Sigma}_{ij}^{total}$ represents a nondimensional combined total stress at any given point in the system, which is a function of the loading parameters ϕ and ω and also of the induced nondimensional micro-stresses $\hat{\sigma}_{ij}^x$, $\hat{\sigma}_{ij}^y$, $\hat{\sigma}_{ij}^{xy}$, and $\hat{\sigma}_{ij}^{th}$. The above nondimensional micro-stresses are obtained via independent 3D finite element solutions of the fundamental boundary value problems aimed at assessing the linear thermo-elastic behavior of the woven morphologies considered in this study. Consistent with the formulation of Equation (13), the individual stress components near the vicinity of large matrix voids shown in Figures 1 and 2 are given by:

$$\begin{aligned}\sigma_{xx}^{total} &= S\hat{\Sigma}_{xx}^{total}\left(\phi,\omega,\beta,\hat{\sigma}_{xx}^x,\hat{\sigma}_{xx}^y,\hat{\sigma}_{xx}^{xy},\hat{\sigma}_{xx}^{th}\right)\\ \sigma_{yy}^{total} &= S\hat{\Sigma}_{yy}^{total}\left(\phi,\omega,\beta,\hat{\sigma}_{yy}^x,\hat{\sigma}_{yy}^y,\hat{\sigma}_{yy}^{xy},\hat{\sigma}_{yy}^{th}\right)\\ \sigma_{zz}^{total} &= S\hat{\Sigma}_{zz}^{total}\left(\phi,\omega,\beta,\hat{\sigma}_{zz}^x,\hat{\sigma}_{zz}^y,\hat{\sigma}_{zz}^{xy},\hat{\sigma}_{zz}^{th}\right)\\ \tau_{xy}^{total} &= S\hat{\Sigma}_{xy}^{total}\left(\phi,\omega,\beta,\hat{\sigma}_{xy}^x,\hat{\sigma}_{xy}^y,\hat{\sigma}_{xy}^{xy},\hat{\sigma}_{xy}^{th}\right)\\ \tau_{xz}^{total} &= S\hat{\Sigma}_{xz}^{total}\left(\phi,\omega,\beta,\hat{\sigma}_{xz}^x,\hat{\sigma}_{xz}^y,\hat{\sigma}_{xz}^{xy},\hat{\sigma}_{xz}^{th}\right)\\ \tau_{yz}^{total} &= S\hat{\Sigma}_{yz}^{total}\left(\phi,\omega,\beta,\hat{\sigma}_{yz}^x,\hat{\sigma}_{yz}^y,\hat{\sigma}_{yz}^{xy},\hat{\sigma}_{yz}^{th}\right)\end{aligned} \tag{14}$$

Matrix cracking initiation: maximum normal stress criterion

According to the normal stress criterion, a given material fails when the maximum normal stress at a point in

the system reaches the ultimate tensile strength of the material. We can then write:

$$\sigma_{p1} = \sigma_{mf} \tag{15}$$

Herein, matrix cracking is assumed to initiate in the isotropic pure CVI SiC matrix regions located between the 0°- and 90°-oriented tows consistent with Morscher.[12] As such, the maximum normal stress criterion is directly applicable, based on the micro-stress distributions in the above regions. In particular, σ_{p1} above, is the maximum normal stress in the CVI SiC matrix, whereas σ_{mf} is the failure stress of *in situ* CVI SiC estimated to be in the range 300–400 MPa. We can obtain σ_{p1} as the biggest eigenvalue of the characteristic equation formed with the stress tensor given by σ_{ij}^{t}. In other words, we solve the characteristic equation:

$$\left|\sigma_{ij}^{t} - \lambda\delta_{ij}\right| = 0 \tag{16}$$

where δ_{ij} is the Kronecker delta taking on a value of 1 if $i=j$ and 0 if $i\neq j$. The stress tensor σ_{ij}^{t} is symmetric with real elements and represents the total induced stress in the vicinity of the matrix voids due to the combined application of each individual in-plane mechanical loading case superimposed with thermal loading as governed by each unique value of β. For a given stress state, Equation (16) yields a cubic characteristic equation for the eigenvalues λ_i, $i=1, 2, 3$. When written in terms of the stress tensor invariants, Equation (16) takes the form:

$$-\lambda^3 + I_t\lambda^2 - II_t\lambda + III_t = 0 \tag{17}$$

where the stress tensor invariants I_t, II_t, and III_t are given by:

$$\begin{aligned} I_t &= \sigma_{xx}^{t} + \sigma_{yy}^{t} + \sigma_{zz}^{t} \\ II_t &= \sigma_{xx}^{t}\sigma_{yy}^{t} + \sigma_{yy}^{t}\sigma_{zz}^{t} + \sigma_{zz}^{t}\sigma_{xx}^{t} - (\sigma_{xy}^{t})^2 - (\sigma_{xz}^{t})^2 - (\sigma_{yz}^{t})^2 \\ III_t &= det(\sigma_{ij}^{t}) \end{aligned} \tag{18}$$

The maximum normal stress σ_{p1} is computed as the biggest root of Equation (17). In terms of the nondimensional matrix micro-stresses Σ_{ij}^{total} given by Equation (13) and the in-plane mechanical loading magnitude S, the maximum normal stress σ_{p1} could be written as:

$$\sigma_{p1} = S\hat{\lambda}_1\left(\hat{\Sigma}_{ij}^{total}\right) \tag{19}$$

where $\hat{\Sigma}_{ij}^{total}$ are the nondimensional matrix micro-stresses due to the combined action of in-plane mechanical loads σ_{xx}^{∞}, σ_{yy}^{∞}, and τ_{xy}^{∞} along with a thermal load resulting from a unit change of the characteristic temperature difference ΔT_c. Also in Equation (19), $\hat{\lambda}_1$ is the largest nondimensional eigenvalue computed from the cubic characteristic Equation (17) formulated with the stress tensor given by $\hat{\Sigma}_{ij}^{total}$. Normalizing Equation (19) with the proportional mechanical load S and invoking the normal stress criterion Equation (15), we derive the functional form of matrix failure Ω_1 given by:

$$\frac{\sigma_{mf}}{S} = \Omega_1\left(\omega, \phi, \beta, \hat{\sigma}_{ij}^{x}, \hat{\sigma}_{ij}^{y}, \hat{\tau}_{ij}^{xy}, \hat{\sigma}_{ij}^{th}\right) \tag{20}$$

Parametric studies presented in the following section of this study, help as to explore the effect of ω, ϕ, and β on Ω_1.

Results

In this section, we will discuss, in detail, the nature of induced micro-stresses in the vicinity of large-scale macroscopic voids in PW and Five Harness satin weave CVI C/SiC CMCs. In addition, the computed profiles of the matrix failure function developed in the previous section and the associated matrix failure loci are also discussed.

As shown in Figure 1, the geometry of the macroscopic voids chosen for stress averaging in this study is morphologically similar in the PW and Four Harness satin weave systems. On the other hand, the geometry of the macroscopic void identified for stress averaging in the Five Harness satin weave morphology is similar to that in the Eight Harness satin weave system. Based on the above similarities, in studies reported elsewhere,[21] it was shown that, while the magnitudes of the micro-stresses, failure functions Ω_1 and predicted failure loci as functions of ω, ϕ, and β are different in the Four Harness and Eight Harness satin weave CVI C/SiC CMCs, their overall functional profiles remain comparable with the PW and Five Harness satin weave morphologies, respectively. Consequently, particular discussions regarding the nature of the micro-stresses, matrix failure functions, and matrix failure loci in the Four Harness and Eight Harness satin weave CVI C/SiC CMCs will not be reported herein, but could be found elsewhere.[21]

Matrix micro-stress profiles

In this study, four different woven CMCs namely, PW, Four Harness, Five Harness, and Eight Harness CVI C/SiC satin weaves were analyzed for their individual PL strengths under the action of combined mechanical and thermal loading. Each of these woven CMCs

presents a different fiber bundle architecture which greatly influences the requisite stress fields. While performing extensive parametric studies, it was observed that the magnitude of the induced stress is not only a function of the constituent material properties but is also dictated by the fiber undulation within the unit-cell.

In studies reported by Haan,[17] it was shown that the woven system reaches its PL strength upon the initiation of matrix cracking. In Haan[17] and in Kuhn et al.[18] a progressive stress-induced micro-cracking damage model is employed to study the stress-induced damage evolution in PW CMC systems. Those studies clearly showed that upon initiation of micro-cracking damage at sites of stress concentration, the apparent stress–strain curve exhibits its first deviation from linearity. The study also showed that the 'knee' of the apparent stress–strain curve becomes more pronounced in systems capable of higher saturation damage densities. In light of the above, the linear fields are employed in this study to identify the end of the linear regime which we define as the PL.

Further, in Haan[17] it was also reported that the most likely site of initiation of matrix cracking is situated around the vicinity of large matrix voids within the domain of the woven unit-cell. For the PW CMC, there is only one large central matrix void which is the site of high-stress concentrations as shown in Figure 1. However, in satin weave CMCs such as the Four, Five, and Eight Harness woven architectures, there are many such discrete matrix voids, all of which act as sites of high-stress concentration. Of the above sites, the matrix void around which the absolute maximum concentration of stress occurs is considered to be the likeliest location for the initiation of first matrix cracking.

In the case of the satin weave morphologies, the highest stress concentrations occur near the vicinity of large matrix voids which are in close proximity to the out-of-plane undulations of fiber tows.[21] Based on this knowledge, the locations of matrix voids where stresses were extracted pursuant to the solution of each boundary value problem over the repeating unit-cells of the Four Harness, Five Harness, and Eight Harness satin weave CMCs are presented in Figures 1(b), 2(a) and (b), respectively.

While computing failure loci for the woven CMCs modeled in this study, we employ averaged stresses near the hole region calculated via detailed 3D finite element solutions. In order to accurately capture the effect of high-stress gradients near the vicinity of matrix voids, stresses are computed at all integration points in all the elements forming the wall of the matrix voids, as shown in Figures 1(c) and 2(c). The average stresses in the void wall are then calculated by first computing the stress at the center of each finite element belonging to the free surface adjacent to the void and then averaging the stresses in the z-direction, in the finite elements at the same angular distance θ relative to the reference x-direction, as shown in Figures 4–9.

Matrix micro-stresses in woven CVI C/SiC CMCs

The profiles of the average micro-stresses computed as discussed above, for the PW and Five Harness satin weave morphologies are presented in Figures 4 and 5, respectively. As shown in the above figures, under mechanical tension along the global X-direction, the $\hat{\sigma}^{x}_{xx}$ stress exhibits a maximum at $\theta = \pm 90^{\circ}$, which for the PW system under consideration is approximately $3.12 \times (1/\hat{E}_{xx}) = 5.15$ times the remotely applied mechanical stress σ^{∞}_{xx}. Similarly, the results in Figure 5(a) indicate that in the Five Harness satin weave C/SiC CMC under consideration, the maximum induced σ^{x}_{xx} stress is of the order of about $2.5 \times (1/\hat{E}_{xx}) = 3.9$ times the remotely applied mechanical load. The normalized effective elastic moduli $\hat{E}_{xx}$ for the PW and Five Harness satin weave C/SiC systems studied herein are listed in Table 2, respectively. These profiles suggest that stress concentrations occur in the void along planes orthogonal to the direction of the applied loading.

The profiles for the stresses resulting from mechanical tension along the global Y-direction are plotted in Figures 4(b) and 5(b) for the PW and Five Harness satin weave CMCs, respectively. The $\hat{\sigma}^{y}_{yy}$ stress which is observed to dominate the stress patterns assumes maximum values at $\theta = \pm 180^{\circ}$ from the reference X-axis. As expected, the results for the stress profiles associated with mechanical tension along the global Y-direction are identical to that obtained for mechanical tension along the global X-direction except that they are 'out-of-phase' by an angular phase shift of $\theta = 90^{\circ}$.

The patterns of the stresses resulting from pure remote shear loading on the C/SiC PW and Five Harness satin weave CMCs under consideration are shown in Figures 4(c) and 5(c), respectively. It may be important to note that the stress profiles reported in the above figures reflect averages along the void wall height obtained at the centroids of the corresponding elements, slightly away from the traction-free wall surface. As such, and while the observed profiles for the normal stresses appear to follow the expected traction-free conditions at the void wall (immediate check can be made at $\theta = 0^{\circ}$ and 90°) the in-plane shear appears to maintain a small nonzero value at the above locations. This result is attributed to the actual location of the element centroid at which the stresses are evaluated.

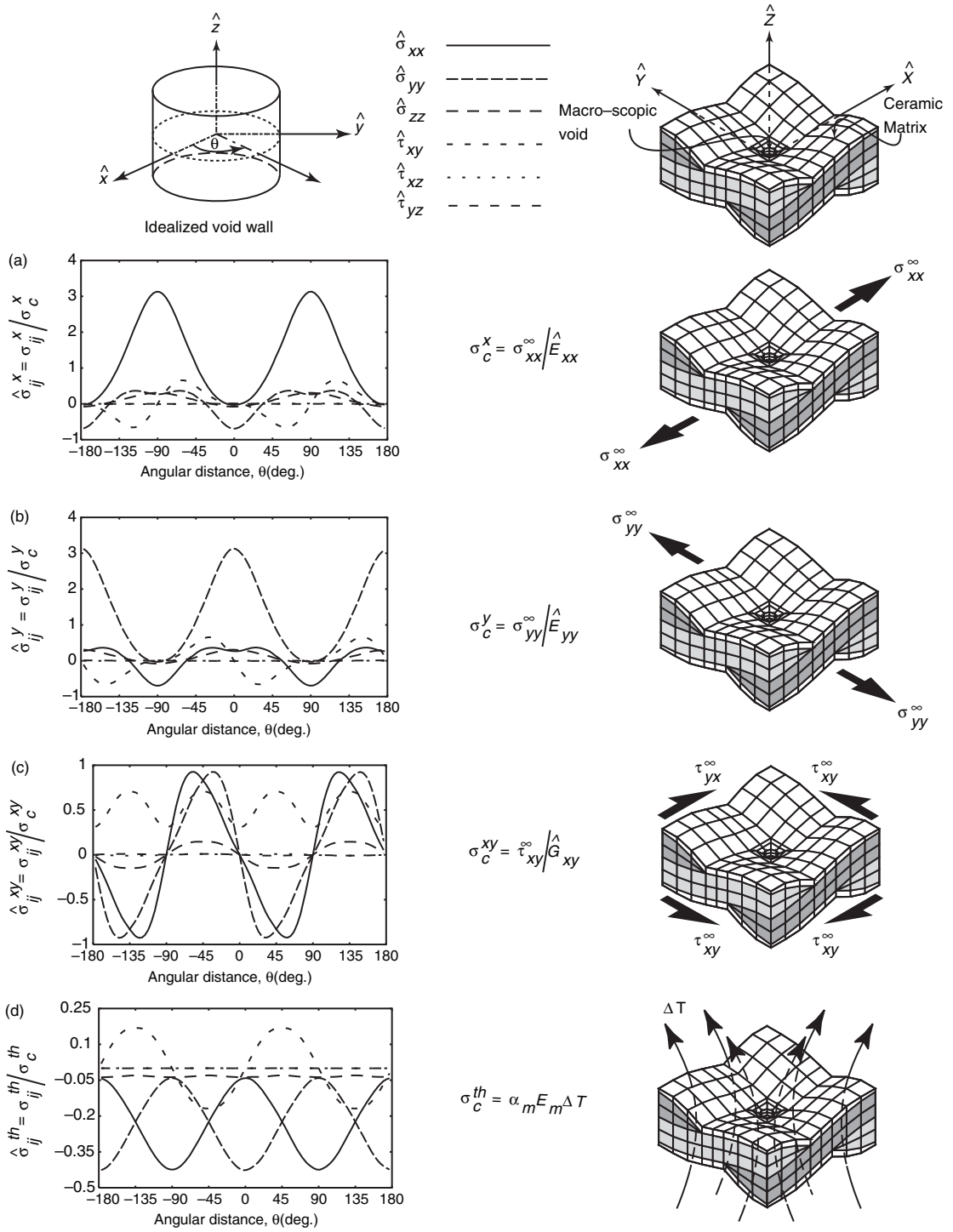

Figure 4. Profiles of the induced normalized matrix micro-stresses in the PW C/SiC CMC near the vicinity of the macroscopic void. (a) Stresses due to tension along the $\hat{X}$-direction ($\omega = 0^\circ$, $\phi = 0^\circ$). (b) Stresses due to tension along the $\hat{Y}$-direction ($\omega = 90^\circ$, $\phi = 0^\circ$). (c) Stresses due to pure remote in-plane shear loading ($\phi = 90^\circ$). (d) Stresses due to free thermal expansion with $\hat{\alpha}_f = \alpha_f/\alpha_m = 0.3$.

With the above limitations in mind, we do observe that at θ offsets of $\pm 45^\circ$, the normal stresses acquire maxima of the order of 0.9 with a nonzero shear of the order of 0.7 in the PW system. The above combination of stresses may result in a maximum principal stress which is estimated to be of the order of $1.7 \times (1/\hat{G}_{xy}) = 7.40$ for the PW and $1.2 \times (1/\hat{G}_{xy}) = 5.15$ for the Five Harness satin weave system. The normalized effective shear moduli $\hat{G}_{xy}$ for the PW and Five Harness satin weave CVI C/SiC

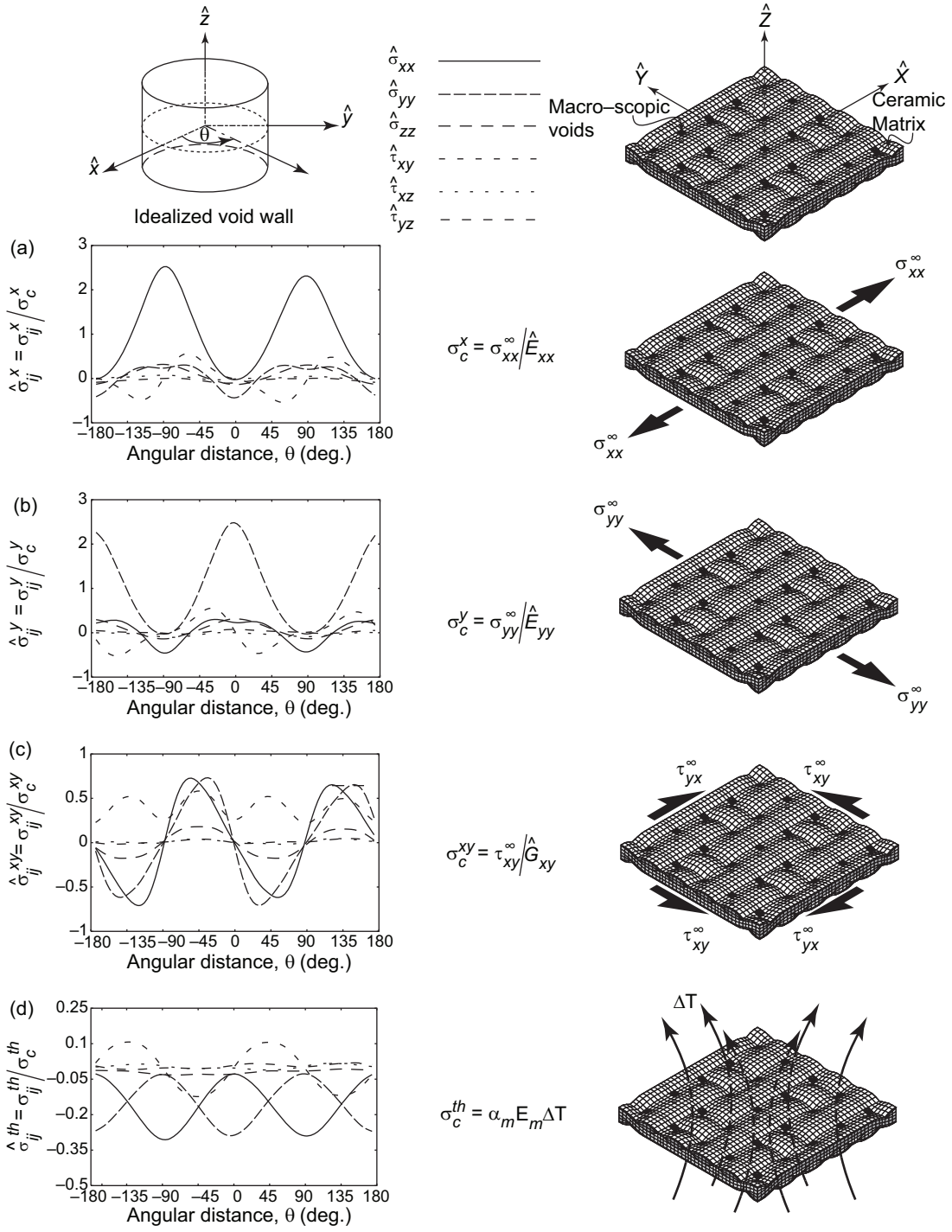

Figure 5. Profiles of the induced normalized matrix micro-stresses in the Five Harness C/SiC CMC near the vicinity of the macroscopic void. (a) Stresses due to tension along the $\hat{X}$-direction ($\omega = 0^\circ$, $\phi = 0^\circ$). (b) Stresses due to tension along the $\hat{Y}$-direction ($\omega = 90^\circ$, $\phi = 0^\circ$). (c) Stresses due to pure remote in-plane shear loading ($\phi = 90^\circ$). (d) Stresses due to free thermal expansion with $\hat{\alpha}_f = \alpha_f / \alpha_m = 0.3$.

systems under consideration are reported in Table 2, respectively.

The stresses induced in the hole region due to free thermal expansion of the PW and Five Harness satin weave C/SiC CMCs are shown in Figures 4(d) and 5(d), respectively. These stresses are driven by the fundamental mismatch in CTEs of the fibers and matrix material. As shown in Table 2 at least for the assumed fiber and

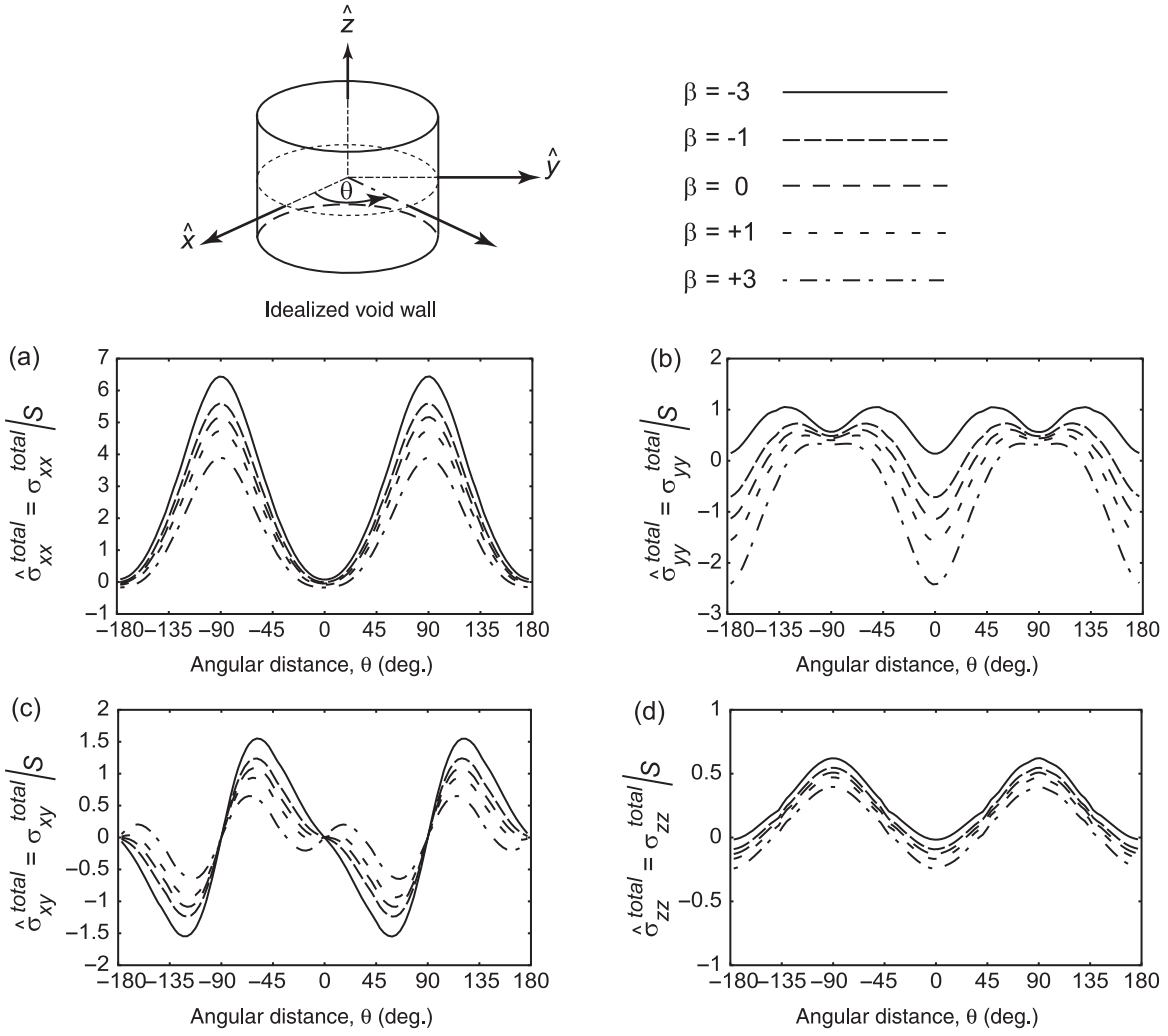

Figure 6. Profiles of the total normalized matrix micro-stresses in the PW C/SiC CMC near the vicinity of the macroscopic void, due to the combined effects of mechanical tension in the $\hat{X}$-direction and thermal loading; i.e., $\omega = \phi = 0^\circ$ and $\beta = -3, -1, 0, +1, +3$. (a) σ_{xx}^{total} stress due to mechanical tension in the $\hat{X}$-direction and thermal loading, (b) σ_{yy}^{total} stress due to mechanical tension in the $\hat{X}$-direction and thermal loading, (c) σ_{xy}^{total} stress due to mechanical tension in the $\hat{X}$-direction and thermal loading, and (d) σ_{zz}^{total} stress due to mechanical tension in the $\hat{X}$-direction and thermal loading.

matrix properties listed in Table 1, the homogenized longitudinal and transverse CTEs of the fiber bundles are much less than the homogenized CTE of the matrix material. As such, the matrix has a tendency to expand more than the fibers for the same positive temperature change ΔT_c, but the fibers tend to restrain the matrix from doing so. Consequently, the matrix is put in a predominantly compressive stress state. The reverse effect is expected when applying a negative temperature change, i.e., the result of cooling during fabrication.

The fundamental nondimensional matrix micro-stresses presented in Figures 4 and 5 bring to light the fact that the magnitude of the normalized stresses induced as a result of mechanical action are appreciably more pronounced in comparison with the normalized stresses induced due to free thermal expansion for a unit change in temperature ΔT_c. Further, the out-of-plane normalized shear stresses $\hat{\tau}_{xz}^{i}$ and $\hat{\tau}_{yz}^{i}$ are negligible in comparison with the other components of stress.

The total stress induced in the vicinity of the matrix void is calculated with the aid of Equation (13) for different values of the thermal-to-mechanical stress ratio β. The effects of β which at least theoretically can take on values from $-\infty$ to $+\infty$ are explored through extensive parametric studies. For a given material system and under a fixed mechanical loading magnitude S, the value of β measures the relative amount of thermal loading given by $\sigma_{th}^{\infty} = E_c \alpha_c \Delta T_c$. More specifically under a constant S, negative values of β capture

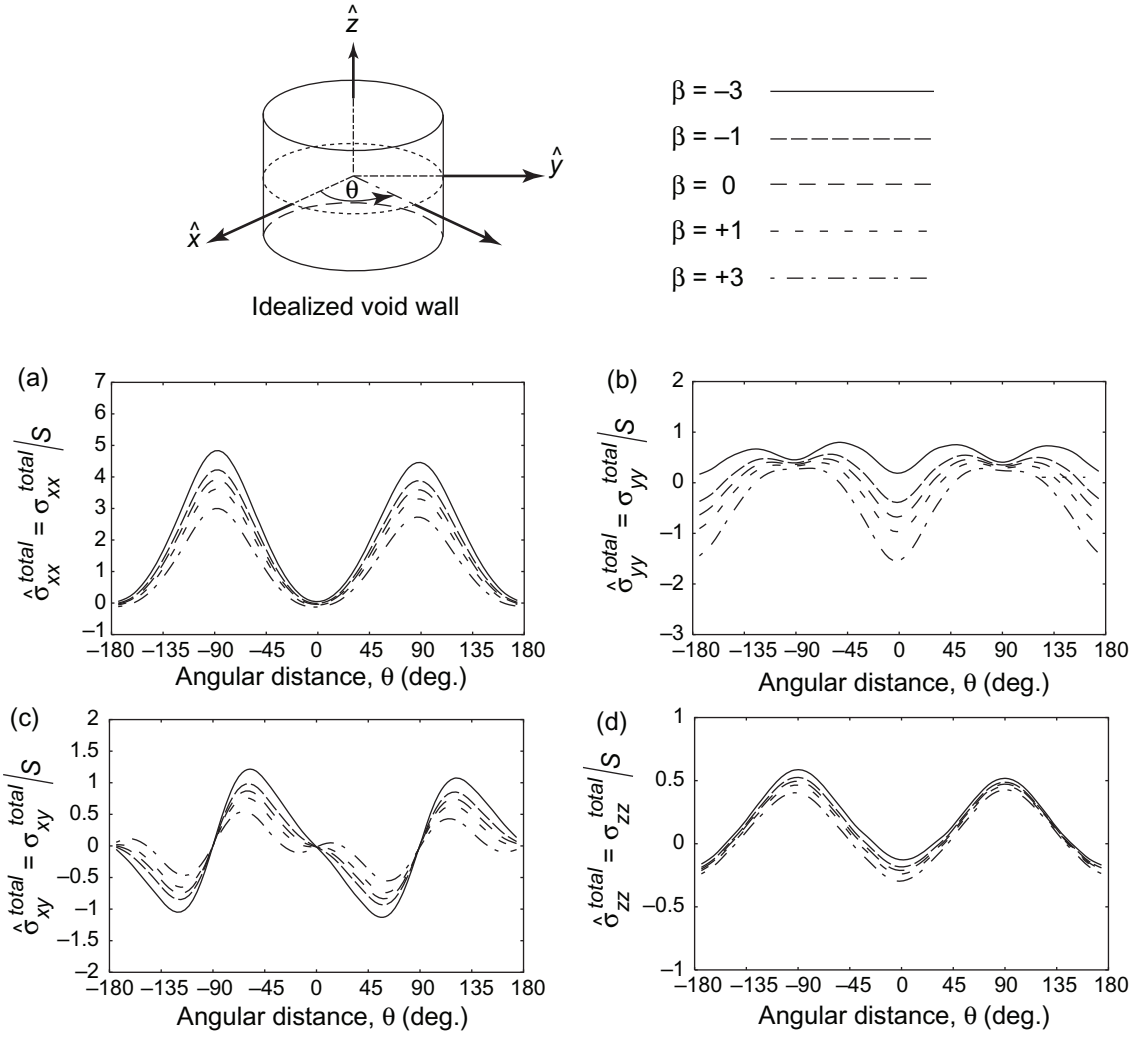

Figure 7. Profiles of the total normalized matrix micro-stresses in the Five Harness C/SiC CMC near the vicinity of the macroscopic void, due to the combined effects of mechanical tension in the $\hat{X}$-direction and thermal loading; i.e., $\omega = \phi = 0^\circ$ and $\beta = -3, -1, 0, +1, +3$. (a) σ_{xx}^{total} stress due to mechanical tension in the $\hat{X}$-direction and thermal loading, (b) σ_{yy}^{total} stress due to mechanical tension in the $\hat{X}$-direction and thermal loading, (c) σ_{xy}^{total} stress due to mechanical tension in the $\hat{X}$-direction and thermal loading, and (d) σ_{zz}^{total} stress due to mechanical tension in the $\hat{X}$-direction and thermal loading.

the case of predominantly thermal loading wherein $\Delta T_c < 0$ whereas positive values of β imply pure thermal loading (if $S = 0$) or predominantly thermal loading with $\Delta T_c > 0$.[26]

In Figure 6, we present the variation of stresses σ_{ij}^{total} where $ij \rightarrow xx$, yy, xy, and zz for values of $\beta = -3$, -1, 0, $+1$, and $+3$ for the PW CVI C/SiC CMC under consideration. The results in Figure 6 were obtained for uniaxial tension along the X-direction ($\omega = 0^\circ$ and $\phi = 0^\circ$) and thermal loading. As shown in the above figure, with $\beta = -3$, $\hat{\sigma}_{xx}^{\max}|_{\theta=\pm 90^\circ} = 6.4$ whereas with $\beta = +3$, $\hat{\sigma}_{xx}^{\max}|_{\theta=\pm 90^\circ} = 3.9$, implying that stress concentrations increase for negative β values and *vice versa*.[26] This result suggests that systems similar to those considered herein and characterized by $\beta < 0$ may exhibit a lower PL stress while also exhibiting increased likelihood of cracking during cooling.[27]

Similarly, the variations of the σ_{ij}^{total} stresses in the Five Harness CVI C/SiC CMC are shown in Figure 7. As shown in the above figure, when $\beta = -3$, $\hat{\sigma}_{xx}^{total}|_{\theta=-90^\circ} = 4.81$ whereas when $\beta = +3$, $\hat{\sigma}_{xx}^{total}|_{\theta=-90^\circ} = 2.98$, once again implying that stress concentrations increase for negative β values and *vice versa*.

The total stress results for uniaxial tension along the Y-direction ($\omega = 90^\circ$ and $\phi = 0^\circ$) and thermal loading would be 'out-of-phase' by 90° with the results presented in Figures 6 and 7. By analogy then, the total stress results due to pure remote in-plane shear ($\phi = 90^\circ$) and thermal loading would be similar to the

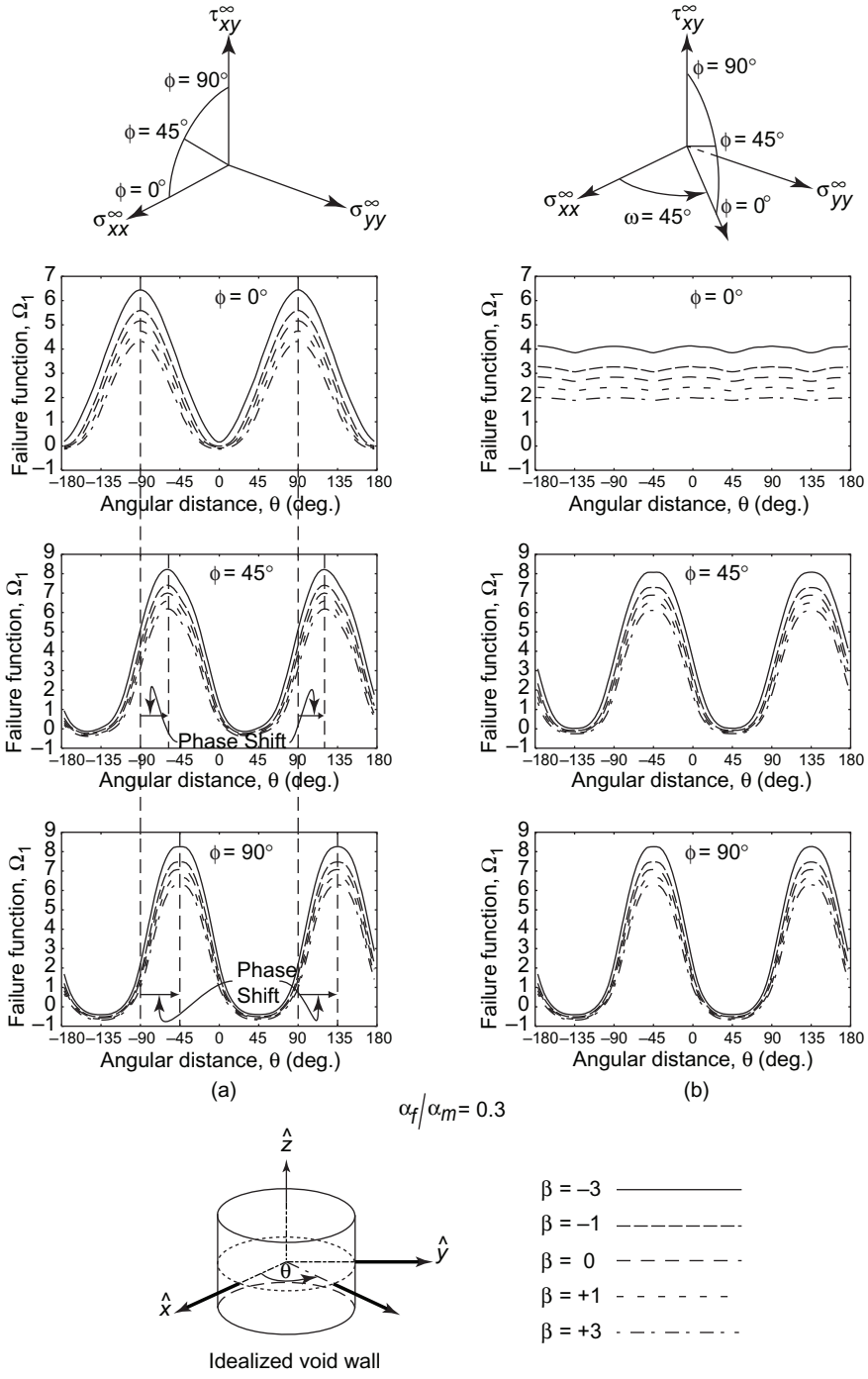

Figure 8. Failure function for PW C/SiC CMC based on the normal stress criterion. Combined effects of remote in-plane mechanical and thermal loading as computed with $\beta = -3, -1, 0, +1, +3$ and $\hat{\alpha}_f = 0.3$. (a) Mechanical tension along the $\hat{X}$-direction ($\omega = 0°$) and increasing amounts of remote in-plane shear ($\phi = 0°$, $\phi = 45°$, $\phi = 90°$). (b) Biaxial tension $\sigma^{\infty}_{xx} = \sigma^{\infty}_{yy}$ ($\omega = 45°$) and increasing amounts of remote in-plane shear ($\phi = 0°$, $\phi = 45°$, $\phi = 90°$).

fundamental matrix micro-stresses due to pure remote in-plane shear.

Overall, the findings regarding the stress fields in woven CMCs considered herein, are consistent with previous research efforts.[17,18] In both works cited above, it was shown that narrow damage bands begin to emanate from the vicinity of macroscopic voids in woven CMCs. These damage sites were also shown to be the most likely locations of initiation of cracking in the matrix material, as also predicted in this study.

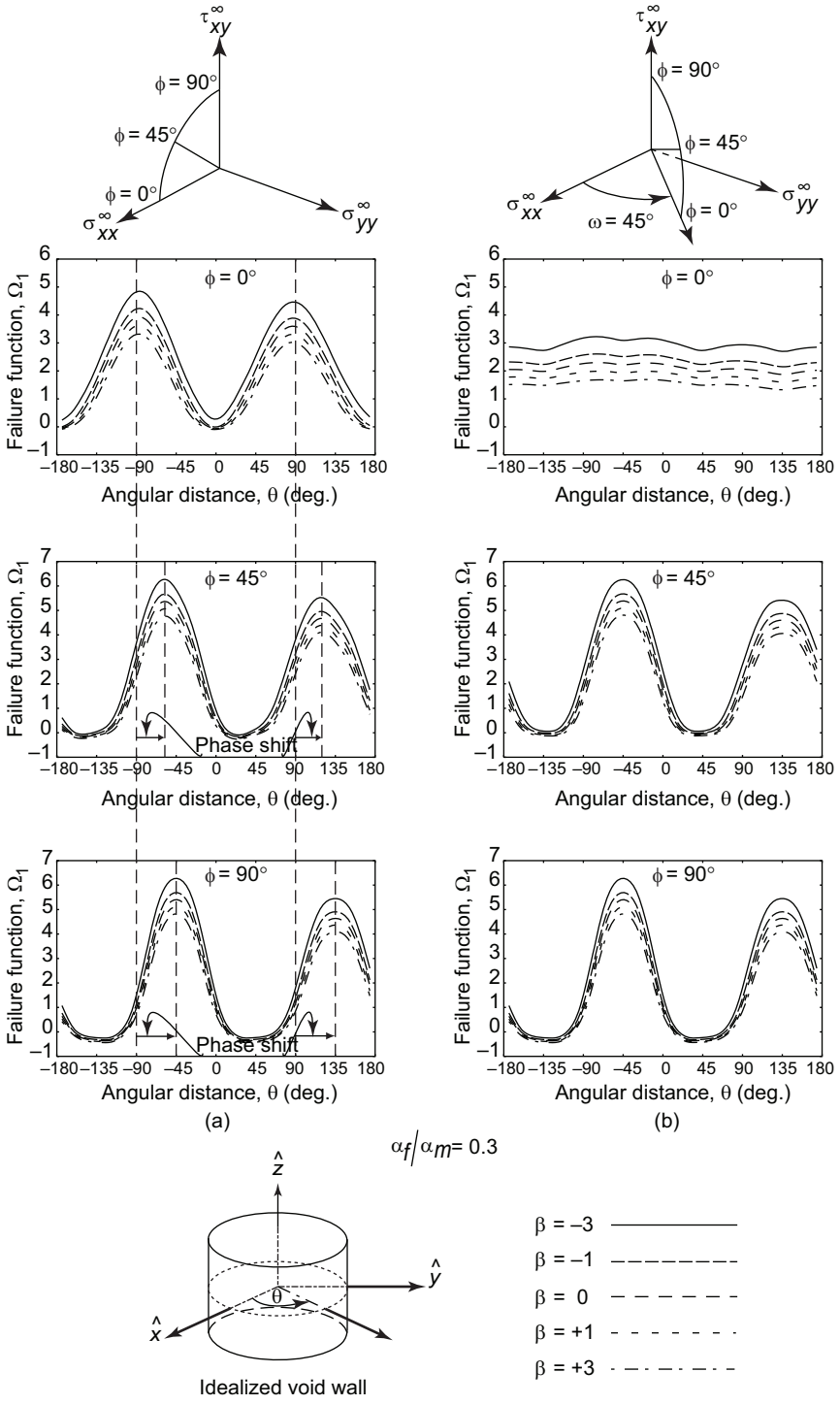

Figure 9. Failure function for the Five Harness C/SiC CMC based on the normal stress criterion. Combined effects of remote in-plane mechanical and thermal loading as computed with $\beta = -3, -1, 0, +1, +3$ and $\hat{\alpha}_f = 0.3$. (a) Mechanical tension along the $\hat{X}$-direction ($\omega = 0^\circ$) and increasing amounts of remote in-plane shear ($\phi = 0^\circ, \phi = 45^\circ, \phi = 90^\circ$) , (b) Biaxial tension $\sigma^{\infty}_{xx} = \sigma^{\infty}_{yy}$ ($\omega = 45^\circ$) and increasing amounts of remote in-plane shear ($\phi = 0^\circ, \phi = 45^\circ, \phi = 90^\circ$).

Matrix failure functions for woven CVI C/SiC CMCs

The effects of ω, ϕ, and β on the failure function Ω_1 for the PW and Five Harness C/SiC CMCs are reported in Figures 8 and 9, respectively. In both the above figures, the left column of plots represents the profiles of Ω_1 as computed for uniaxial tension along the X-direction ($\phi = 0^\circ$ and $\omega = 0^\circ$) and different thermal loading conditions along with increasing amounts of pure remote in-plane shear load ($\phi = 0^\circ$, $\phi = 45^\circ$, $\phi = 90^\circ$). On the other hand, the right column of plots shown in Figures 8 and 9 reports on the profiles of Ω_1 due to biaxial tension ($\sigma_{xx}^{\infty} = \sigma_{yy}^{\infty}$ since $\omega = 45^\circ$) and the above-mentioned thermal and additional in-plane shear loads. To be consistent with the results presented for $\hat{\sigma}_{ij}^{total}$ in Figures 6 and 7, we present here results obtained for Ω_1 with $\beta = -3$, -1, 0, $+1$, and $+3$. As expected, the failure function takes on maximum values as for $\beta < 0$ regardless of the value of either ω or ϕ. As seen from Figures 8(a) and (b) and 9(a) and (b), for individual levels of β, the magnitudes of the failure function Ω_1 increases along with the relative amount of in-plane shear loading as measured via the parameter ϕ. This behavior suggests that the matrix is more susceptible to cracking under the action of combined in-plane mechanical shear and thermal loading in comparison with remote in-plane mechanical tension and thermal loading.

Also as evident from Figures 8(a) and 9(a), the failure function Ω_1 attains maximum values at $\theta = \pm 90^\circ$ from the reference x-axis. This remains true for uniaxial tension along the X-direction ($\omega = 0^\circ$) combined with thermal loading conditions as computed through the parameter β and in the absence of any remote in-plane mechanical shear load ($\phi = 0^\circ$). However, with increasing amounts of in-plane shear coupled with uniaxial tension along the X-direction and thermal loading, the angular positions of the maxima and minima exhibited by Ω_1 shift to the right as indicated by the dotted vertical lines through the left column of plots in Figures 8(a) and 9(a). This result implies that the likely location of matrix crack initiation shifts to the right as the relative amount of remote in-plane shear load increases.

The profiles of Ω_1 under the combined action of remote biaxial tension ($\sigma_{xx}^{\infty} = \sigma_{yy}^{\infty}$ since $\omega = 45^\circ$) and increasing amounts of in-plane shear load and changing thermal environment as measured via the parameter β are presented in Figures 8(b) and 9(b), which clearly indicate the absence of any 'phase shift' as witnessed in Figures 8(a) and 9(a). These profiles of Ω_1 suggest that failure is most likely to initiate at 'equatorial' void planes regardless of the value of either ω or ϕ.

However, in the Five Harness woven system, Ω_1 exhibits maxima corresponding to $\theta < 0$, consistent with the total stress results in Figure 7. As such, it is likely that matrix cracking in the Five Harness CMC might first initiate in the 'equatorial' plane of the matrix void in the region $\theta < 0$ regardless of the combined values of ω, ϕ and β.

Estimates of PL strength. The above-mentioned failure function could be employed to obtain independent estimates of the PL strengths of woven CVI C/SiC CMCs under different loading conditions which is given by,

$$S = \frac{\sigma_{mf}}{\Omega_1^{\max}(\beta)} \tag{21}$$

In Equation (21), σ_{mf} is the CVI SiC matrix failure stress and $\Omega_1^{\max}(\beta)$ is determined from the results reported in Figure 8. The results in Table 3 list the predicted PL strengths for the PW CVI C/SiC CMC system under consideration under uni-axial, bi-axial, pure shear, and general planar loads in the absence of thermal loading ($\beta = 0$). Similarly, using Equation (21), independent estimates of the PL strengths of the Five Harness satin weave CVI C/SiC CMCs studied herein could be obtained, as illustrated in Table 4.

The above results indicate that the PL strength of C/SiC CMCs depends on the weave architecture of the reinforcing fibers. Studies by Morscher et al.,[12,28,29] Camus et al.,[27] and Holmes,[30] confirm the above observation and also indicate the strong dependence of the PL strength on micro-constituent content. Therefore, it becomes difficult to exhaustively corroborate the PL strength results for the model CVI C/SiC systems considered herein. However, consistent with Morsher,[12] systems with higher undamaged elastic modulus are reported to be characterized by a higher PL strength, as shown in Tables 3 and 4.

Furthermore, as seen from Tables 3 and 4, the predicted biaxial strength is greater than the uniaxial strength for the PW and 5HS woven C/SiC CMCs. In a system wherein stress concentrates around holes/voids, this study, in tandem with classical elasticity suggests that due to remote tension in say, the X-direction, a stress concentration factor dominates the σ_{xx} stress at the equatorial plane perpendicular to the axis of loading. On the other hand, a compressive σ_{yy} stress develops at the poles relative to the loading axis. As such, the application of a second remote stress perpendicular to the first, in this case σ_{yy}, will have a stress relief effect at the equatorial points. Thus, higher applied stresses are required for failure in the latter case as indeed is predicted by this model. The stress profiles shown in Figures 4 and 5 can be used for further clarification of this point.

Table 3. Comparison of predicted and experimentally established first matrix cracking stress values of PW C/SiC CMC under different loading conditions. These results were obtained assuming the tensile strength of CVI SiC matrix σ_{mf} as 400 MPa

	Uniaxial tension ($\omega = 0°$, $\phi = 0°$)	Biaxial tension ($\omega = 45°$, $\phi = 0°$)	Pure shear ($\omega = 0°$, $\phi = 90°$)	General loading ($\omega = 45°$, $\phi = 45°$)
Applied stress	$\sigma_{xx}^{\infty} = S$	$\sigma_{xx}^{\infty} = S/\sqrt{2}$ $\sigma_{yy}^{\infty} = S/\sqrt{2}$	$\tau_{xy}^{\infty} = S$	$\sigma_{xx}^{\infty} = S/2$ $\sigma_{yy}^{\infty} = S/2$ $\tau_{xy}^{\infty} = S/\sqrt{2}$
σ_{ij}^{∞}	$\beta = 0$	$\beta = 0$	$\beta = 0$	$\beta = 0$
Maximum normal stress criterion $\Omega_1 = \sigma_{mf}/S$	5.14	2.85	6.68	6.52
CVI SiC tensile strength σ_{mf}	400	400	400	400
Matrix cracking stress (MPa) $S_1 = \sigma_{mf}/\Omega_1$	$S_1 = 77.82$ $\sigma_{xx}^{\infty} = 77.82$	$S_1 = 140.35$ $\sigma_{xx}^{\infty} = 99.24$ $\sigma_{yy}^{\infty} = 99.24$	$S_1 = 59.88$ $\tau_{xy}^{\infty} = 59.88$	$S_1 = 61.35$ $\sigma_{xx}^{\infty} = 30.67$ $\sigma_{yy}^{\infty} = 30.67$ $\tau_{xy}^{\infty} = 43.38$
Reported data (MPa) $S_1 = \sigma_{mf}/\Omega_1$	80 (Haan[17])	NA	NA	NA

Table 4. Predicted first matrix cracking stress of Five Harness C/SiC CMC under different loading conditions. These results were obtained assuming the tensile strength of CVI SiC matrix σ_{mf} as 400 MPa

	Uniaxial tension ($\omega = 0°$, $\phi = 0°$)	Biaxial tension ($\omega = 45°$, $\phi = 0°$)	Pure shear ($\omega = 0°$, $\phi = 90°$)	General loading ($\omega = 45°$, $\phi = 45°$)
Applied stress	$\sigma_{xx}^{\infty} = S$	$\sigma_{xx}^{\infty} = S/\sqrt{2}$ $\sigma_{yy}^{\infty} = S/\sqrt{2}$	$\tau_{xy}^{\infty} = S$	$\sigma_{xx}^{\infty} = S/2$ $\sigma_{yy}^{\infty} = S/2$ $\tau_{xy}^{\infty} = S/\sqrt{2}$
σ_{ij}^{∞}	$\beta = 0$	$\beta = 0$	$\beta = 0$	$\beta = 0$
Maximum normal stress criterion $\Omega_1 = \sigma_{mf}/S$	3.9	2.3	5.12	5.12
CVI SiC tensile strength σ_{mf}	400	400	400	400
Matrix cracking stress (MPa) $S_1 = \sigma_{mf}/\Omega_1$	$S_1 = 102.56$ $\sigma_{xx}^{\infty} = 102.56$	$S_1 = 173.91$ $\sigma_{xx}^{\infty} = 122.97$ $\sigma_{yy}^{\infty} = 122.97$	$S_1 = 78.125$ $\tau_{xy}^{\infty} = 78.125$	$S_1 = 78.125$ $\sigma_{xx}^{\infty} = 39.06$ $\sigma_{yy}^{\infty} = 39.06$ $\tau_{xy}^{\infty} = 55.24$
Reported data (MPa) $S_1 = \sigma_{mf}/\Omega_1$	NA	NA	NA	NA

Matrix failure loci for woven CVI C/SiC CMCs

In order to further understand the effects of applied mechanical and thermal loads on the matrix cracking failure stress, matrix failure loci for the current woven C/SiC CMCs are developed. The proportional loading vector $S = \sigma_{xx}^{\infty}\hat{i} + \sigma_{yy}^{\infty}\hat{j} + \tau_{xy}^{\infty}\hat{k}$ was employed along with the loading proportionality constant β to develop profiles of the failure function Ω_1, as discussed in the previous section. The maxima $\Omega_1^{\max}(\beta)$ exhibited by Ω_1 discussed above were used to develop failure envelops or loci in the normalized $\hat{\sigma}_{xx}^{\infty} - \hat{\tau}_{xy}^{\infty}$ space for different combinations of ω and ϕ. Therefore, for a given remotely applied mechanical load controlled by the spherical loading parameters ω and ϕ, the matrix would fail in accordance with the normal stress criterion if:

$$\begin{aligned} \frac{\sigma_{xx}^{\infty}}{\sigma_{mf}} &> \frac{\cos\phi\cos\omega}{\Omega_1^{\max}(\beta)} \\ \frac{\tau_{xy}^{\infty}}{\sigma_{mf}} &> \frac{\sin\phi}{\Omega_1^{\max}(\beta)} \end{aligned} \tag{22}$$

where $\Omega_1^{\max}(\beta)$ implies that the maxima exhibited by Ω_1 is a function of the loading proportionality constant β.

Figures 10(a) and 11(a) show the predicted failure loci for the PW and Five Harness satin weave C/SiC systems under the combined action of remote in-plane mechanical tension along the X-direction and thermal loading as measured via the parameter β, respectively. In Figure 10(b–d), we show predicted failure loci for the PW C/SiC CMC under changing thermal environment and increasing amounts of remote biaxial tension $\omega = 15^{\circ}$, $\omega = 30^{\circ}$, and $\omega = 45^{\circ}$, respectively. Similarly, Figure 11(b–d) shows the predicted failure loci for the Five Harness C/SiC CMC under changing thermal environment and increasing amounts of remote biaxial tension $\omega = 15^{\circ}$, $\omega = 30^{\circ}$, and $\omega = 45^{\circ}$, respectively.

The results presented in Figure 10 suggest that under mechanical loads (i.e. $\beta = 0$), the failure locus intersects the x-axis at a distance equal to approximately 1.25 times the y-axis intercept. This suggests that first matrix cracking may initiate more readily under pure shear compared to pure tension loading.

The above effect is somewhat lesser in systems with residual thermal stresses with negative values of the β loading parameter. At the same time, in systems with positive β values, this effect is amplified considerably resulting in failure loci which are more elongated along the σ_{xx}^{∞}-axis of loading, as shown in Figure 10. The above observation derived from the failure loci results reported in Figure 10 suggest that first matrix cracking may initiate more readily under the combined effects of remote mechanical shear and thermal loading compared to the combined effects of remote mechanical tension and thermal loading.

For a given combination of ω and β, as $\phi \to 0^{\circ}$:

$$\sigma_{ij}^{total} \to S\left[\left(\frac{1}{\hat{E}_{xx}}\right)\cos\omega\hat{\sigma}_{ij}^{x} + \left(\frac{1}{\hat{E}_{yy}}\right)\sin\omega\hat{\sigma}_{ij}^{y} + \beta\hat{\sigma}_{ij}^{th}\right] \tag{23}$$

On the other hand, when $\phi \to 90^{\circ}$:

$$\sigma_{ij}^{total} \to S\left[\left(\frac{1}{\hat{G}_{xy}}\right)\hat{\sigma}_{ij}^{xy} + \beta\hat{\sigma}_{ij}^{th}\right] \tag{24}$$

The failure loci results reported in Figure 10 depend on the maxima $\Omega_1^{\max}(\beta)$ (Equation (22)) exhibited by the failure function Ω_1, which in turn are a function of the total induced stress as derived in Equation (20). Furthermore, the relative magnitudes of $\hat{\sigma}_{ij}^{x}$ and $\hat{\sigma}_{ij}^{y}$ are far greater than $\hat{\sigma}_{ij}^{xy}$ and $\hat{\sigma}_{ij}^{th}$, as shown in Figure 4. For negative β values (i.e. $\Delta T_c < 0$) and $0 \le \phi \le 90^{\circ}$, the maxima $\Omega_1^{\max}(\beta)$ progressively increases, as shown in Figure 8. However, since $\hat{E}_{xx}$ and $\hat{E}_{yy}$ are greater than $\hat{G}_{xy}$ (Table 2) $|\Omega_1^{\max}(\beta)|_{\phi\to 0^{\circ}} < |\Omega_1^{\max}(\beta)|_{\phi\to 90^{\circ}}$, consistent with Equations (23) and (24). Therefore, the failure loci shrink for negative β values and the combination of pure remote shear and thermal loads becomes more detrimental than the combination of pure remote tension and thermal loads. The opposite effects would be expected for positive β values, resulting in the elongated failure loci shown in Figure 10. In general, the woven CVI C/SiC composite systems are susceptible to cracking during cooling from the curing to the room temperatures, i.e., for $\Delta T < 0$ and consequently $\beta < 0$, as also reported in Camus et al.[27]

Further, the results in Figure 10 indicate that for negative β values, matrix cracking is predicted to initiate at lower remotely applied mechanical loads. This result implies that at higher temperature changes ($\Delta T_c < 0$), the apparent PL strength of the PW C/SiC CMC decreases apparently due to increased tensile thermal stresses in the matrix phase induced by the large mismatch in the CTEs of the fibers and matrix material. These characteristics give rise to elliptical failure loci shown in Figure 10 for any given combination of ω and β. The observations made above are consistent with the results reported for the failure function Ω_1 in Figure 8 and also the fundamental micro-stresses presented in Figure 4 and the total induced stress profiles presented in Figure 6.

The tensile PL strength of the PW C/SiC CMC reported in Table 1(Panel C), when normalized with respect to the CVI SiC matrix failure stress of

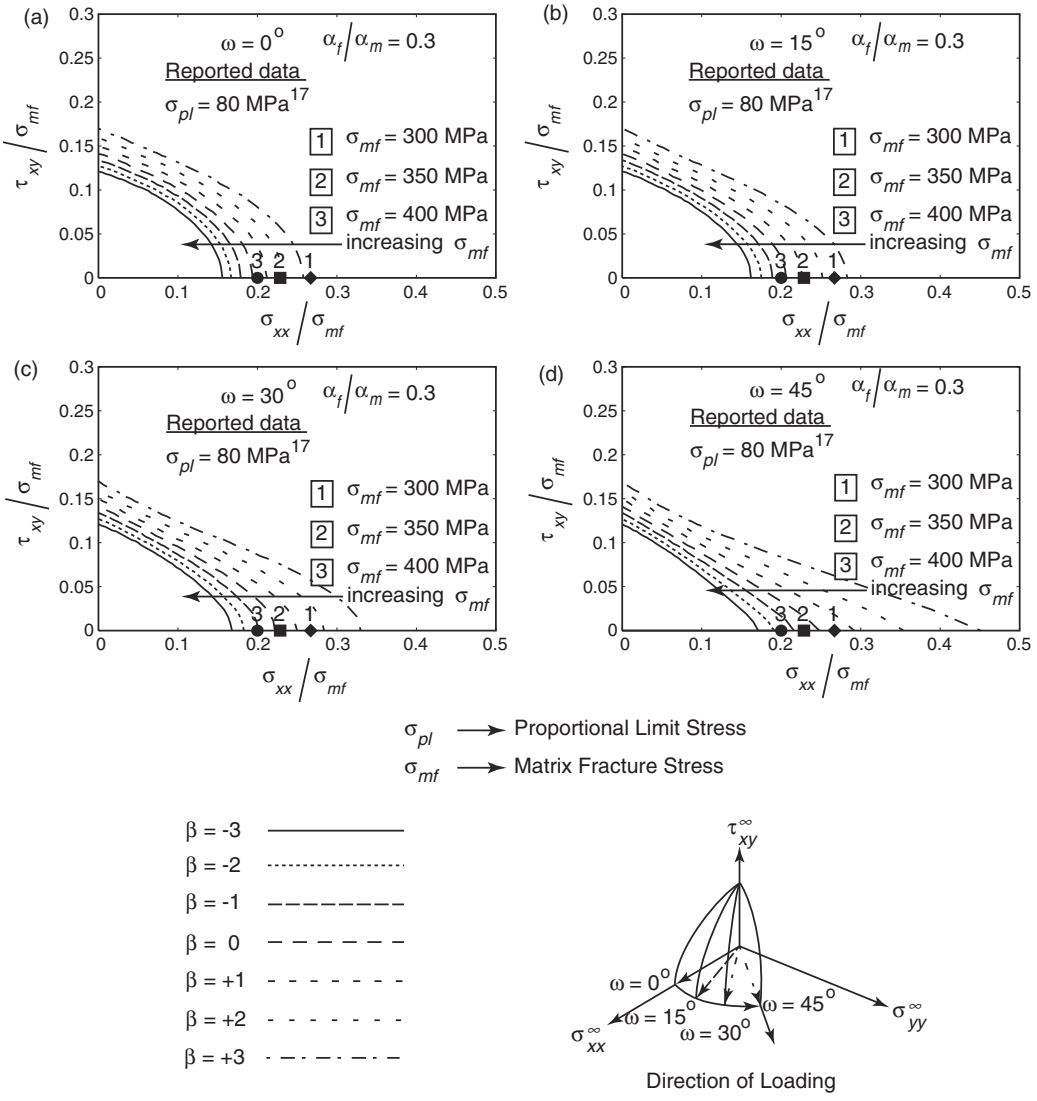

Figure 10 Matrix failure loci for the PW C/SiC CMC based on the normal stress criterion, computed under the combined action of in-plane mechanical loads and changing thermal environment as measured via $\beta = -3, -2, -1, 0, +1, +2, +3$. (a) Uniaxial tension along the $\hat{X}$-direction ($\phi = 0^\circ$ and $\omega = 0^\circ$). (b) Combined mechanical tension along the $\hat{X}$- and $\hat{Y}$-directions ($\phi = 0^\circ$ and $\omega = 15^\circ$). (c) Combined mechanical tension along the $\hat{X}$- and $\hat{Y}$-directions ($\phi = 0^\circ$ and $\omega = 30^\circ$). (d) Biaxial tension $\sigma_{xx}^{\infty} = \sigma_{yy}^{\infty}$ ($\phi = 0^\circ$ and $\omega = 45^\circ$).

$\sigma_{mf} = 300$–400 MPa, and superimposed on the failure loci, results in the three discrete failure points shown in Figure 10(a). As such, within the context of the above-estimated σ_{mf}, model predictions completely envelop experimental data.

As could be inferred from Figure 11, the matrix cracking failure loci of the Five Harness C/SiC composite system are comparable, at least qualitatively, to those of the PW C/SiC system. However, note that for the same change in temperature ΔT, the results in Figure 11 indicate that tensile and shear loads of greater magnitudes are required for matrix cracking to initiate in the Five Harness C/SiC CMC than the PW CMC system. This result is consistent with the finding that the magnitude of the stress concentration factor as measured via the parameter $\Omega_1^{\max}(\beta)$ in Figures 8 and 9 is lesser in the Five Harness CMC than in the PW CMC, for any given combination of ω, ϕ, and β.

Discussion

This study focused on evaluating the failure behavior of complex woven plain and satin weave C/SiC CMCs, under the combined action of general in-plane mechanical loads and thermal environments resulting from changes in temperature ΔT. During the cooling of CMCs from the stress-free processing to room

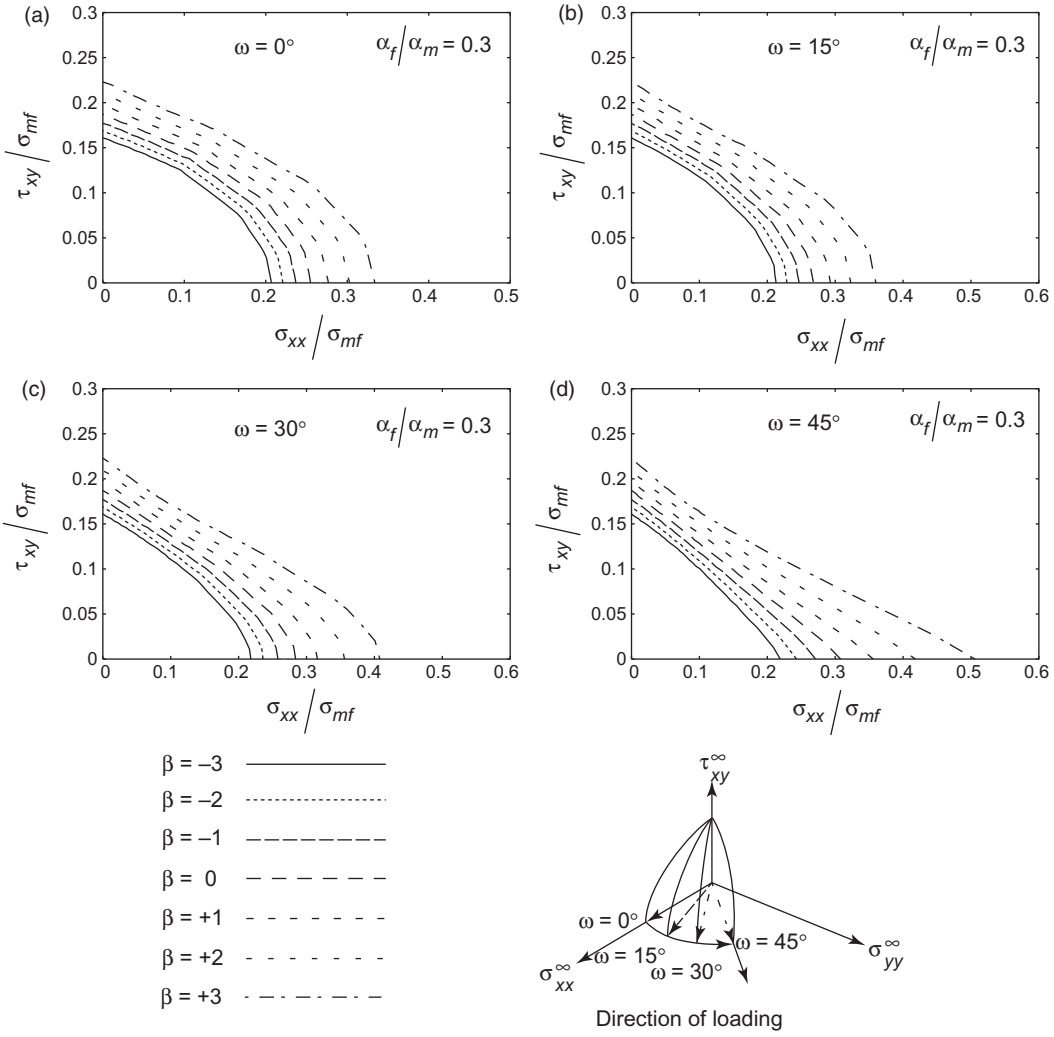

Figure 11. Matrix failure loci for the Five Harness C/SiC system based on the normal stress criterion, computed under the combined action of in-plane mechanical loads and changing thermal environment as measured via $\beta = -3, -2, -1, 0, +1, +2, +3$. (a) Uniaxial tension along the $\hat{X}$-direction ($\phi = 0^\circ$ and $\omega = 0^\circ$). (b) Combined mechanical tension along the $\hat{X}$- and $\hat{Y}$-directions ($\phi = 0^\circ$ and $\omega = 15^\circ$). (c) Combined mechanical tension along the $\hat{X}$- and $\hat{Y}$-directions ($\phi = 0^\circ$ and $\omega = 30^\circ$). (d) Biaxial tension $\sigma^{\infty}_{xx} = \sigma^{\infty}_{yy}$ ($\phi = 0^\circ$ and $\omega = 45^\circ$).

temperatures, the matrix material shrinks differentially from the reinforced fiber tows giving rise to thermal residual stresses as well as dispersed micro-porosity and large-scale voids. Although Chapman and Whitcomb[31] have advocated that modeling these large-scale pores could be computationally expensive, it has been clearly shown in previous studies[17,18] that these large matrix pores are discontinuities in an otherwise continuous medium and as such act as sites of high-stress concentration. By computing the stresses concentrations near the vicinity of these matrix voids and incorporating these stresses in a failure criterion based on maximum normal stress, matrix failure loci aimed at assessing the first matrix cracking stress corresponding to the PL of these woven CMCs have been developed.

It has been reported in the study by Morscher[12] on 2D woven melt-infiltrated SiC/SiC composites that cracking of the matrix initiated outside of the load bearing mini-composite. In fact, Morscher[12] hypothesized that all the matrix cracks originated in the 90° tow regions or the large SiC–Si pure matrix regions. It should be noted herein that the hypothesis in Morscher[12] points to the matrix-rich regions between the 0° and 90° tows and not the 90° bundles *per se*. In the current matrix cracking model it was shown that matrix voids present in the above-mentioned regions act as sites of high-stress concentrations,

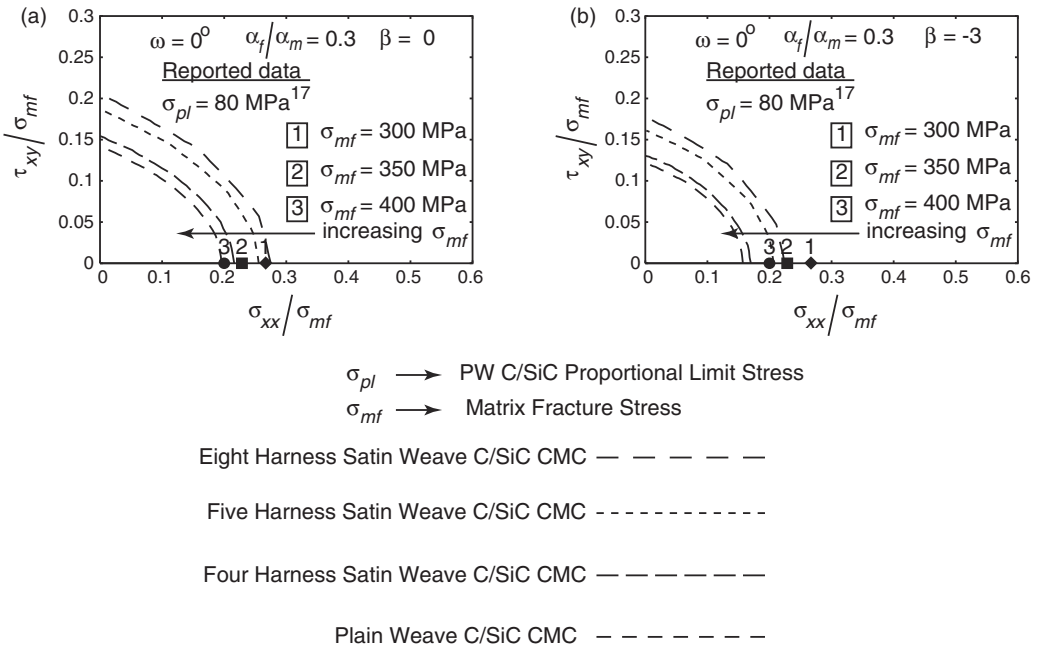

Figure 12. Failure loci of the PW and Four, Five, and Eight Harness Satin Weave C/SiC CMCs based on the normal stress criterion. (a) Comparison of the failure loci under remote mechanical tension in the $\hat{X}$-direction ($\omega = 0^\circ$ and $\phi = 0^\circ$) in the absence of any thermal load ($\beta = 0$). (b) Comparison of the failure loci under remote mechanical tension in the $\hat{X}$-direction ($\omega = 0^\circ$ and $\phi = 0^\circ$) subjected to severe thermal loading ($\beta = -3$).

thereby forming the most likely regions of matrix crack initiation. Furthermore, in this study, the rather arbitrary geometry of the processing-induced macroscopic voids were modeled as complex geometry occupying the space between the lower matrix layer of one ply and the upper matrix layer of its adjacent ply, through a cylindrical hole.[20] While further modeling may be needed to quantify the effects of the inter-connecting hole shape and size, the consistency of the predicted results when compared to albeit, limited experimental data, reinforce confidence in the modeling approach developed.

Comparison of tensile PL data of the PW C/SiC CMC obtained from Haan[17] with model predictions as reported in Figure 10, inspires confidence in the finite element model developed in this study. Figure 12(a) displays the failure loci of the PW and Four, Five, and Eight Harness C/SiC CMCs under uniaxial mechanical tension ($\omega = 0^\circ$) and in the absence of any thermal load ($\beta = 0$), while Figure 12(b) reports on the failure loci of the above woven morphologies under severe thermal loading ($\beta = -3$). It is evident from Figure 12 that under a given combination of mechanical and thermal loading, approximately equal amounts of mechanical tensile loads are required to initiate matrix cracking in pure tension in both the PW and Four Harness Satin Weave CMCs. However, the Five and Eight Harness satin weave C/SiC CMCs appear to present a slightly higher resistance to matrix cracking in pure shear as well as pure tension, under any given mechanical and thermal loading environment.

Limitations of the thermal analysis

At typical processing temperatures of C/SiC CMCs (1200–1500°C Trinquecoste et al.[32]), the longitudinal CTE of the T300 carbon fibers is usually bounded as $1.2 \times 10^{-6}/^\circ\text{C} \leq \alpha_L^f \leq 1.9 \times 10^{-6}/^\circ\text{C}$. On the other hand, the radial (transverse) CTE of the T300 fibers decreases from $17.6 \times 10^{-6}/^\circ\text{C}$ in the temperature range 25–200°C to $1.2 \times 10^{-6}/^\circ\text{C}$ around 600–800°C.[33] There seems to be an unavailability of the transverse (α_T^f) CTE of T300 carbon fibers beyond 800°C; as such, in this study, $\alpha_T^f = \alpha_L^f = \alpha_f$. In particular, the CTE of the T300 carbon fibers is set as $\alpha_f = 1.2 \times 10^{-6}/^\circ\text{C}$, while the CTE of the CVI SiC matrix is taken to be $\alpha_m = 4.0 \times 10^{-6}/^\circ\text{C}$. Consequently, the parametric studies reported in this study that explore the effects of thermal loads on the first cracking stress in woven CMCs are limited to the case when $\hat{\alpha}_f = \alpha_f/\alpha_m = 0.3$. As such, the failure loci presented in this study do not fully capture the thermal stress effects over a broad range of fiber and matrix CTEs. Potentially, one could solve several different thermal load boundary value problems with individual values of α_L^f and α_T^f, and develop a broad array of failure loci. Such studies, while computationally

demanding, would yield model data that would readily present an environment for assessing the effects of fiber and matrix CTE mismatch.

Due to unavailability of appropriate data and the CVI technique of matrix deposition, in these studies, we assume that the CTE of micro-constituent phases such as the fiber coating, bundle matrix, and bundle coating are equal to that of the inter-bundle matrix. This assumption presents another limitation on the thermal analysis performed in this study. Therefore, the complete set of results encompassing effects of thermal loads would require solutions to multiple finite element boundary value problems. In each of these simulations, the CTEs of the micro-constituent phases would need to be appropriately chosen to reflect actual composite systems.

Conclusions

A robust modeling framework for the quantification of stress concentrations around large-scale voids and their effects on the PL strength of woven CMCs under remotely applied in-plane mechanical loads and different thermal environments has been developed. The detailed geometry models of woven CMCs employed in this study accurately capture the local stress distribution around the vicinity of macroscopic matrix voids.

The stress concentrations around these matrix voids in the PW C/SiC CMCs were shown to be 5.14 times greater than the remotely applied mechanical loads under uniaxial tension ($\omega = 0^\circ$) and in the absence of any thermal loads ($\beta = 0$). With increasing temperature changes, the thermal stresses appear to play a greater role most likely leading to a degradation in the apparent high temperature first cracking strength of woven CMCs.

Satin weave CMCs such as the Four, Five, and Eight Harness morphologies pose a greater modeling challenge. However, the robust geometry models of these woven CMCs developed in Rao et al.[20] account for high-stress concentrations near discrete matrix voids in the weave resulting during processing. Employing the same methodology as developed for the PW CMCs, stress concentrations of magnitudes 4.8, 3.9, and 3.61 were computed for the Four, Five, and Eight Harness C/SiC CMCs, respectively, under uniaxial mechanical tension and in the absence of any thermal loads. Further, it was also shown that in harsher thermal environments ($\beta < 0$), the magnitude of the computed tensile normal stress concentrations increases with increasing cooling ΔT and *vice versa*.

Based on the results presented in the previous sections, it could be predicted that satin weave CMCs would require higher mechanical and thermal loads to initiate matrix cracking than the PW CMCs, provided the material micro-constituent properties are the same. However, more substantive comparisons with experimentally established temperature sensitive failure data for woven CMCs are needed for model validation.

Acknowledgment

Support for this study was provided by Technology Assessment and Transfer (TAT) and Ceramic Composites, Inc. (CCI) through an STTR - US Air Force subcontract.

References

1. Ishikawa T and Chou T-W. Stiffness and strength behavior of woven fabric composites. *J Mater Sci* 1982; 17: 3211–3220.
2. Ishikawa T and Chou T-W. In-plane thermal expansion and thermal bending coefficients of fabric composites. *J Compos Mater* 1983; 17: 92–104.
3. Ishikawa T and Chou T-W. One-dimensional micromechanical analysis of woven fabric composites. *AIAA J* 1983; 21(12): 1714–1721.
4. Naik NK and Shembekar PS. Elastic behavior of woven fabric composites: I-lamina analysis. *J Compos Mater* 1992; 26(15): 2196–2225.
5. Naik RA. Analysis of woven and braided fabric reinforced composites. Technical report, NASA, June 1994.
6. Naik RA. Failure analysis of woven and braided fabric reinforced composites. *J Compos Mater* 1995; 29(17): 2334–2363.
7. Naik RA, Ifju PG and Masters JE. Effect of fiber architecture parameters on deformation fields and elastic moduli of 2-D braided composites. *J Compos Mater* 1995; 28(7): 656–681.
8. Vandeurzen Ph, Ivens J and Verpoest I. A Three-dimensional micromechanical analysis of woven- fabric composites: I. geometric analysis. *Compos Sci Technol* 1996; 56: 1303–1315.
9. Vandeurzen Ph, Ivens J and Verpoest I. A Three-dimensional micromechanical analysis of woven- fabric composites: II. elastic analysis. *Compos Sci Technol* 1996; 56: 1317–1327.
10. Cox BN and Flanagan G. Handbook of analytical methods for textile composites. Technical report, NASA, 1997.
11. Whitcomb JD and Tang X. Effective moduli of woven composites. *J Compos Mater* 2001; 35(23): 2127–2144.
12. Morscher GN. Stress-dependent matrix cracking in 2D woven SiC-fiber reinforced melt-infiltrated SiC matrix composites. *Compos Sci Technol* 2004; 64: 1311–1319.
13. Morscher GN. Modeling the elastic modulus of 2D woven CVI SiC composites. *Compos Sci Technol* 2006; 66(15): 2804–2814.
14. Lamon J, Lissart N, Rechiniac C, Roach DH and Jouin JM. Micromechanical and statistical approach to the behavior of CMCs. *Ceram Eng Sci Proc* 1993; 14: 1115–1124.
15. Aubard X, Lamon J and Allix O. Model of the nonlinear mechanical behavior of 2D SiC-SiC chemical vapor

infiltration composites. *J Am Ceram Soc* 1994; 77(8): 2118–2126.
16. Singh RN. Fracture and crack growth in ceramic matrix composites at high temperatures. Presented at the 106th Annual Meeting and Exposition of the American Ceramic Society, Indianapolis, IN, 2004.
17. Haan SI. Modeling of the mechanical response of plain weave composites. PhD thesis, The University of Maryland, 2000.
18. Kuhn JL, Haan SI and Charalambides PG. Stress induced matrix microcracking in brittle matrix plain weave fabric composites under uniaxial tension. *J Compos Mater* 2000; 34(19): 1640–1664.
19. Smith CE, Morscher GN and Xia ZH. Monitoring damage accumulation in ceramic matrix composites using electrical resistivity. *Scr Mater* 2004; 59: 463–466.
20. Rao MP, Pantiuk M and Charalambides PG. Modeling the geometry of satin weave fabric composites. *J Compos Mater* 2009; 43(1): 19–56.
21. Rao MP. Modeling the thermo-mechanical elastic response of plain and satin weave composites. PhD thesis, The University of Maryland, 2005.
22. Chamis CC. Simplified composite micromechanics equations for hygral, thermal and mechanical properties. Technical report, NASA: TM 83320, 1983.
23. Kuhn JL and Charalambides PG. Elastic response of porous matrix plain weave fabric composites: Part I-modeling. *J Compos Mater* 1998; 32(16): 1426–1471.
24. Kuhn JL and Charalambides PG. Elastic response of porous matrix plain weave fabric composites: Part II-results. *J Compos Mater* 1998; 32(16): 1472–1507.
25. Kuhn JL, Haan SI and Charalambides PG. A semi-analytical method for the calculation of the elastic microfields in plain weave fabric composites subjected to in-plane loading. *J Compos Mater* 1999; 33(3): 221–266.
26. Rao MP, Pantiuk M and Charalambides PG. Initiation of matrix cracking in woven ceramic matrix composites. Ceramic Transactions 165. In: *Proceedings of the 106th Annual General Meeting and Exposition of the American Ceramic Society*, Indianapolis, IN, 2004, pp.165–180.
27. Camus G, Guillaumat L and Baste S. Development of damage in a 2D woven C/SiC composite under mechanical loading: I. Mechanical characterization. *Compos Sci Technol* 1996; 56: 1363–1372.
28. Morscher GN, Yun HM and DiCarlo JA. In-plane cracking behavior and ultimate strength for 2D woven and braided melt-infiltrated SiC/SiC composites tensile loaded in off-axis fiber directions. *J Am Ceram Soc* 2007; 90(10): 3185–3193.
29. Morscher GN, DiCarlo JA, Kiser JD and Yun HM. Effects of fiber architecture on matrix cracking for melt-infiltrated SiC/SiC composites. *Int J Appl Ceram Technol* 2010; 7(3): 276–290.
30. Holmes JW. Influence of loading frequency on the fatigue behavior of fiber-reinforced ceramic composites. Department of Mechanical Engineering and Applied Mechanics, The University of Michigan, Ann Arbor, MI 48109 Final Technical Report, Contract # – F49620-95-1-0206, Directorate of Chemistry and Materials Science, Air Force Office of Scientific Research, Bolling Air Force Base, DC, 1997.
31. Chapman CD and Whitcomb JD. Thermally induced damage initiation and growth in plain and satin weave carbon-carbon composites. *Mech Compos Mater Struct* 2000; 7: 177–194.
32. Trinquecoste M, Carlierm JL, Derré A, Delhaès P and Chadeyron P. High temperature thermal and mechanical properties of high tensile carbon single filaments. *Carbon* 1996; 34(7): 923–929.
33. Shindo A. Polyacrylonitrile (PAN)-based carbon fibers. In: Kelly A and Zweben C (eds) *Comprehensive composite materials*. Oxford: Elsevier Science Ltd, 2000, Vol. 1, pp.1–33.